COMMUN. MATH. SCI.
Vol. 22, No. 4, pp. 871–910

ACCURATE DETERMINISTIC PROJECTION METHODS FOR STIFF DETONATION WAVES*

ALINA CHERTOCK†, SHAOSHUAI CHU‡, AND ALEXANDER KURGANOV§

Abstract. We study numerical approximations of the reactive Euler equations of gas dynamics. In addition to shock, contact and rarefaction waves, these equations admit detonation waves appearing at the interface between different fractions of the reacting species. It is well-known that in order to resolve the reaction zone numerically, one has to take both space and time stepsizes to be proportional to the reaction time, which may cause the numerical method to become very computationally expensive or even impractical when the reaction is fast. Therefore, it is necessary to develop underresolved numerical methods, which are capable of accurately predicting locations of the detonation waves without resolving their detailed structure. One can distinguish between two different degrees of stiffness. In the *stiff* case, the reaction time is very small, while in the *extremely stiff* case, the reaction is assumed to occur instantaneously.

In [A. KURGANOV, in Hyperbolic problems: theory, numerics, applications, Springer, Berlin, 2003], we proposed a simple underresolved method—an accurate deterministic projection (ADP) method—for one-dimensional hyperbolic systems with stiff source terms including the reactive Euler equations in the extremely stiff regime. In this paper, we extend the ADP method to the (non-extremely) stiff case, multispecies detonation models, and the two-dimensional reactive Euler equations in all of the aforementioned regimes. We also investigate ways to distinguish between different regimes in practice as well as study the limitations of the proposed ADP methods with respect to the ignition temperature. We demonstrate the accuracy and robustness of the ADP methods in a number of numerical experiments with both relatively low and large ignition temperature, and illustrate the difficulties one may face when the ignition temperature is low.

Keywords. Stiff detonation waves; reactive Euler equations; splitting method; deterministic projection method; central-upwind scheme; multispecies detonation.

AMS subject classifications. 76M12; 65M08; 76V05; 35L65; 35L67.

1. Introduction

We study numerical methods for hyperbolic systems of balance laws with very stiff source terms. In the two-dimensional (2-D) case, such systems read as

$$\boldsymbol{U}_t+\boldsymbol{F}(\boldsymbol{U})_x+\boldsymbol{G}(U)_y=\boldsymbol{S}(\boldsymbol{U},\varepsilon),\tag{1.1}$$

where, $\boldsymbol{U}$ is an unknown function of space variables x and y and a time variable t, $\boldsymbol{F}$ and $\boldsymbol{G}$ are given flux functions and $\boldsymbol{S}$ is a source term, which depends on the stiffness parameter $0<\varepsilon\ll 1$. In particular, we consider an inviscid, compressible, reacting flow, governed by the reactive Euler equations, which, in the single reaction case, have the

*Received: February 21, 2022; Accepted (in revised form): September 07, 2023. Communicated by Giovanni Russo.

†Department of Mathematics, North Carolina State University, Raleigh, NC 27695, USA (chertock@math.ncsu.edu).

‡Department of Mathematics and Shenzhen International Center for Mathematics, Southern University of Science and Technology, Shenzhen, 518055, China (chuss2019@mail.sustech.edu.cn).

§Department of Mathematics, Shenzhen International Center for Mathematics and Guangdong Provincial Key Laboratory of Computational Science and Material Design, Southern University of Science and Technology, Shenzhen, 518055, China (alexander@sustech.edu.cn).

following form:

$$\begin{pmatrix}\rho\\ \rho u\\ \rho v\\ E\\ \rho z\end{pmatrix}_t+\begin{pmatrix}\rho u\\ \rho u^2+p\\ \rho uv\\ u(E+p)\\ \rho uz\end{pmatrix}_x+\begin{pmatrix}\rho v\\ \rho uv\\ \rho v^2+p\\ v(E+p)\\ \rho vz\end{pmatrix}_y=\begin{pmatrix}0\\ 0\\ 0\\ 0\\ -\rho zK(\tau;\varepsilon,\tau_c)\end{pmatrix}. \tag{1.2}$$

Here, the dependent variables ρ, u, v, E and z are the density, x- and y-velocities, total energy and the fraction of unburnt gas, respectively. The system is completed through the following equation of state (EOS):

$$p=(\gamma-1)\left[E-\frac{\rho}{2}(u^2+v^2)-q_0\rho z\right], \tag{1.3}$$

where the parameters γ and q_0 represent the specific heat ratio and chemical heat release, respectively. On the right-hand side (RHS) of (1.2), $\tau:=p/\rho$ is the temperature. Finally, the reaction can be modeled by either the Arrhenius kinetic term,

$$K(\tau;\varepsilon,\tau_c)=\frac{1}{\varepsilon}e^{-\tau_c/\tau}, \tag{1.4}$$

where τ_c is the ignition temperature and ε is the reaction time, or even stiffer Heaviside kinetic term [34]:

$$K(\tau;\varepsilon,\tau_c)=\frac{1}{\varepsilon}H(\tau-\tau_c)=\begin{cases}\dfrac{1}{\varepsilon}, & \text{if } \tau\geq\tau_c,\\ 0, & \text{otherwise.}\end{cases} \tag{1.5}$$

The system (1.2)–(1.3) with the kinetic term $K(\tau;\varepsilon,\tau_c)$ given by either (1.4) or (1.5) is a hyperbolic system of balance laws whose solutions contain shock, contact and rarefaction waves. In addition, in the studied stiff regimes, it also admits detonation waves appearing at the interface between the burnt and unburnt fractions of the gas. It is well-known that in order to resolve the reaction zone numerically, one has to take both spatial $(\Delta x,\Delta y)$ and temporal (Δt) stepsizes to be proportional to the reaction time ε, which may cause the numerical method to become very computationally expensive or even impractical when the reaction is fast, that is, when $\Delta x/\varepsilon\gg 1$, $\Delta y/\varepsilon\gg 1$ and $\Delta t/\varepsilon\gg 1$. Therefore, it is necessary to develop underresolved numerical methods, which are capable of accurately predicting locations of the detonation waves without resolving their detailed structure. One can distinguish between two different degrees of stiffness. In the *stiff* case ($\varepsilon\ll 0$), the reaction time is very small, while in the *extremely stiff* regime ($\varepsilon\to 0$), the reaction is assumed to occur instantaneously. In the latter case, the reaction can only be modeled by the stiffer Heaviside kinetic term (1.5).

Designing an accurate underresolved numerical method for the general system (1.1) with a very small ε (or, in particular, for the reactive Euler system in either stiff or extremely stiff regime) is a rather challenging task. Since the system is stiff, it is natural that one may wish to use an operator splitting (fractional step) method; see, e.g., [23,26,29]. The latter can be implemented by considering the following two subsystems:

$$\boldsymbol{U}_t+\boldsymbol{F}(\boldsymbol{U})_x+\boldsymbol{G}(\boldsymbol{U})_y=\boldsymbol{0} \tag{1.6}$$

and

$$\boldsymbol{U}_t=\boldsymbol{S}(\boldsymbol{U},\varepsilon). \tag{1.7}$$

Then, assuming that $\boldsymbol{U}(x,t)$ is available at time t, an approximate solution at the next time level $t+\Delta t$ is given by

$$\boldsymbol{U}(x,y,t+\Delta t)=S_{\mathcal{P}}(\Delta t)S_{\mathcal{H}}(\Delta t)\boldsymbol{U}(x,y,t),$$

where $S_{\mathcal{H}}$ and $S_{\mathcal{P}}$ denote the solution operators for the subsystems (1.6) and (1.7), respectively.

The hyperbolic system of conservation laws (1.6) can be solved by any (stable and sufficiently accurate) shock-capturing method. In this paper, we use the second-order central-upwind scheme briefly described in the Appendix. Central-upwind schemes are Riemann-problem-solver-free Godunov-type schemes for general multidimensional hyperbolic systems of conservation laws. These schemes were first proposed in [20] and then further developed in [17–19, 21].

The step of solving the ODE (1.7) requires a special attention. In the extremely stiff case, the solution operator $S_{\mathcal{P}}$ reduces to the projection of the computed solution onto an equilibrium state:

$$\boldsymbol{U}\mapsto\mathcal{P}\boldsymbol{U}, \tag{1.8}$$

where $\boldsymbol{S}(\mathcal{P}\boldsymbol{U},\varepsilon)\equiv\boldsymbol{0}$. In a less stiff case, one has to solve the ODE (1.7) with a very small, yet finite ε. Though this solution may be very close to the projected one given by (1.8), the difference between the stiff and extremely stiff cases is sometimes significant, especially in the multispecies case considered in Section 4.

Even though the operator splitting method is very simple, it has a major drawback: If the deterministic projection operator described in Section 2.1 is used in (1.8), this approach may lead to a spurious weak detonation wave that travels with a nonphysical propagation speed (the same phenomena will be observed if the ODE (1.7) is solved in the case of a very small ε). This occurs since shock-capturing methods smear discontinuities, and as soon as the nonphysical value of the temperature in this numerical layer is above the ignition temperature, a certain part of the gas may get numerically burnt prematurely. This peculiar numerical phenomenon was first observed in [8, 9], and since then it has attracted lots of attention. It was found in [22] that the propagation error is mainly due to numerical dissipation, and in order to tackle this numerical problem, it was reduced in, e.g., [38]. In [6, 7, 25, 35], front-tracking approaches were used to obtain the correct propagation of the reactive front. Since numerical dissipation cannot be generally avoided, alternative approaches that focus on establishing accurate temperatures from the artificially diffused solutions have been proposed: the ignition temperature was artificially increased in [5], corrected [12, 28], or replaced using random projection methods [2, 3, 31]. Numerical methods using overlapping grids and block-structured adaptive mesh refinement for high-speed reactive flow in complex geometries were proposed in [13, 14]. In [32, 33, 36], the ENO subcell approach was utilized to design high-order finite-difference methods. In [37], the threshold values method, which is based on the physically motivated detonation wave velocities correction, was proposed. We refer the reader to [4, 31, 32, 36–38] for the extensions of some of the aforementioned numerical methods to the case of multispecies detonation.

A simple and robust alternative to the aforementioned approaches was proposed in [16], where an accurate deterministic projection (ADP) method for one-dimensional (1-D) hyperbolic systems with extremely stiff source terms was introduced. The key idea of the ADP method for the reactive Euler equations can be described as follows. In order to avoid numerical smearing of the profile of z, we only solve the equations for the density, momentum and energy at the hydrodynamics substep $S_{\mathcal{H}}$. The values of z

are then evolved in time only during the projection substep $S_{\mathcal{P}}$, at which the pressure (and hence the temperature) is computed using the EOS, at which the values of z from the previous time level are used; see the details presented in the 2-D case in Section 2.2.

In this paper, we generalize the ADP method developed in [16] for the 1-D extremely stiff reactive Euler equations to the 2-D case and to the following settings. First, in Section 3, we consider the single reaction case in the non-extremely stiff regime with either Arrhenius (1.4) or Heaviside (1.5) kinetic terms and replace the projection operator (1.8) with a trapezoidal-like ODE solver. We then consider in Section 4 the multispecies detonation, for which we either directly extend the ADP solution operator (in the extremely stiff regime; Section 4.1) or develop a special ADP-based ODE solver (in the non-extremely stiff regime; Section 4.2). These extensions are carried out in both the 1-D and 2-D cases. The developed ADP methods are tested on a number of numerical examples, presented in Section 2.3, Section 3.1 and Section 4.3 at the end of each section after the corresponding version of the ADP method is presented. In the conducted numerical experiments, we compare the obtained numerical solutions with the corresponding reference solutions computed by a fully resolved central-upwind scheme, and outline ways to distinguish between different regimes in practice. In addition, we study the limitations of the ADP methods with respect to the ignition temperature τ_c and demonstrate the accuracy and robustness of the proposed ADP method in a number of numerical experiments with relatively large τ_c. We also illustrate the difficulties one may face when τ_c is low.

2. Deterministic projection method: extremely stiff case

In this section, we describe two deterministic projection approaches for solving the reactive Euler Equations (1.2)–(1.3), (1.5) in an extremely stiff regime.

2.1. "Standard" deterministic projection (SDP) method. We begin with a "standard" deterministic projection (SDP) approach. For simplicity, we consider a rectangular computational domain covered by a uniform spatial mesh consisting of the cells $C_{j,k}$ centered at $(x_j,y_k):=(j\Delta x,k\Delta y)$ and assume that the computed solution is realized in terms of its cell averages, $\overline{\boldsymbol{U}}^n_{j,k}=\frac{1}{\Delta x\Delta y}\int_{C_{j,k}}\boldsymbol{U}(x,y,t^n)\,dy\,dx$, and available at time level $t=t^n$. In order to evolve the solution to the next time level according to the aforementioned operator splitting approach, we first use a (stable and accurate) shock-capturing method to numerically solve the homogeneous system arising at the hydrodynamics substep (1.6):

$$\begin{pmatrix}\rho\\ \rho u\\ \rho v\\ E\\ \rho z\end{pmatrix}_t+\begin{pmatrix}\rho u\\ \rho u^2+p\\ \rho uv\\ u(E+p)\\ \rho uz\end{pmatrix}_x+\begin{pmatrix}\rho v\\ \rho uv\\ \rho v^2+p\\ v(E+p)\\ \rho vz\end{pmatrix}_y=\begin{pmatrix}0\\0\\0\\0\\0\end{pmatrix},\tag{2.1}$$

completed through the EOS (1.3). Here, we prefer to work with finite-volume methods (in particular, with the central-upwind scheme described in the Appendix), but would like to stress that the considered computational framework is general and may be used in conjunction with one's favorite shock-capturing method. The cell averages $\overline{\rho}^{n+1}_{j,k}$, $(\overline{\rho u})^{n+1}_{j,k}$, $(\overline{\rho v})^{n+1}_{j,k}$, $\overline{E}^{n+1}_{j,k}$ and $(\overline{\rho z})^{*}_{j,k}$ at the new time level $t^{n+1}:=t^n+\Delta t$ are then used to obtain $u^{n+1}_{j,k}=(\overline{\rho u})^{n+1}_{j,k}/\overline{\rho}^{n+1}_{j,k}$, $v^{n+1}_{j,k}=(\overline{\rho v})^{n+1}_{j,k}/\overline{\rho}^{n+1}_{j,k}$, $z^{*}_{j,k}:=(\overline{\rho z})^{*}_{j,k}/\overline{\rho}^{n+1}_{j,k}$ and to define

$$p^{n+1}_{j,k}(z)=(\gamma-1)\left[\overline{E}^{n+1}_{j,k}-\frac{\overline{\rho}^{n+1}_{j,k}}{2}\left((u^{n+1}_{j,k})^2+(v^{n+1}_{j,k})^2\right)-q_0\overline{\rho}^{n+1}_{j,k}z\right]\tag{2.2}$$

and

$$\tau_{j,k}^{n+1}(z)=\frac{p_{j,k}^{n+1}(z)}{\overline{\rho}_{j,k}^{n+1}}. \tag{2.3}$$

Notice that for the $(\overline{\rho z})_{j,k}^{*}$ and $z_{j,k}^{*}$ the upper index is not $n+1$ yet as they are going to be changed after the projection step (1.8), at which we obtain the values of z and ρz at time level $t=t^{n+1}$:

$$z_{j,k}^{n+1}=\begin{cases}0, \text{ if } \ \tau_{j,k}^{n+1}(z_{j,k}^{*})\geq\tau_c,\\ 1, \text{ if } \ \tau_{j,k}^{n+1}(z_{j,k}^{*})<\tau_c,\end{cases}\qquad (\overline{\rho z})_{j,k}^{n+1}=\overline{\rho}_{j,k}^{n+1}z_{j,k}^{n+1},$$

and then calculate $p_{j,k}^{n+1}(z_{j,k}^{n+1})$ using (2.2) with $z=z_{j,k}^{n+1}$.

This "standard" deterministic projection method is very simple, but as mentioned in Section 1 it may lead to spurious, nonphysical detonation waves traveling with artificial speeds, which makes the "standard" deterministic projection method impractical. Utilizing the ADP method presented in the next section allows one to avoid such an undesirable situation.

2.2. Accurate deterministic projection (ADP) method. The main reason of the failure of the SDP method is that it uses nonphysical, artificial values of $(\overline{\rho z})_{j,k}^{*}$ obtained after the fluid dynamics substep $S_{\mathcal{H}}$ of the operator splitting method. The simplest way to prevent this undesirable situation is not to solve the (ρz)-equation at the fluid dynamics step at all. We thus modify the deterministic projection method as follows.

Once again, we assume that cell averages of the solution at time level $t=t^n$ (including the values of the fraction of unburnt gas $z_{j,k}^{n}=(\overline{\rho z})_{j,k}^{n}/\overline{\rho}_{j,k}^{n}$) have been already computed. We first evolve them in time by applying a (stable and accurate) shock-capturing finite-volume method to the homogeneous system that contains only the first four equations of the system (2.1):

$$\begin{pmatrix}\rho\\ \rho u\\ \rho v\\ E\end{pmatrix}_t+\begin{pmatrix}\rho u\\ \rho u^2+p\\ \rho uv\\ u(E+p)\end{pmatrix}_x+\begin{pmatrix}\rho v\\ \rho uv\\ \rho v^2+p\\ v(E+p)\end{pmatrix}_y=\begin{pmatrix}0\\0\\0\\0\end{pmatrix}, \tag{2.4}$$

completed through the EOS (1.3). As before, the evolved cell averages $\overline{\rho}_{j,k}^{n+1}$, $(\overline{\rho u})_{j,k}^{n+1}$, $(\overline{\rho v})_{j,k}^{n+1}$ and $\overline{E}_{j,k}^{n+1}$ (but not $(\overline{\rho z})_{j,k}^{*}$, which is not computed now at all) are used to obtain $u_{j,k}^{n+1}$, $v_{j,k}^{n+1}$ and $p_{j,k}^{n+1}(z_{j,k}^{n})$ using (2.2) with $z=z_{j,k}^{n}$. Notice that compared with the SDP method, the pressure $p_{j,k}^{n+1}$ is now computed using the value of z from the previous time level, which is one of the crucial points in the ADP method.

The projection step is then performed as in the case of the SDP method, but with $\tau_{j,k}^{n+1}(z_{j,k}^{*})$ replaced with $\tau_{j,k}^{n+1}(z_{j,k}^{n})$, namely, we set

$$z_{j,k}^{n+1}=\begin{cases}0, \text{ if } \ \tau_{j,k}^{n+1}(z_{j,k}^{n})\geq\tau_c,\\ 1, \text{ if } \ \tau_{j,k}^{n+1}(z_{j,k}^{n})<\tau_c,\end{cases} \tag{2.5}$$

where $\tau_{j,k}^{n+1}(z_{j,k}^{n})$ is computed using (2.2), (2.3) with $z=z_{j,k}^{n}$.

Upon the completion of the projection step (2.5), we calculate $p_{j,k}^{n+1}(z_{j,k}^{n+1})$ using (2.2) with $z=z_{j,k}^{n+1}$.

2.3. Numerical examples. In this section, we demonstrate the performance of the proposed ADP method and compare it with the SDP method on four 2-D numerical examples. For the 1-D numerical examples, we refer the reader to [16].

In the first three examples, we take the CFL number 0.5 (the time step Δt is determined adaptively by using the CFL condition for the homogeneous systems (2.4) and (2.1) for the ADP and SDP methods, respectively), while in the fourth example we use a smaller CFL number 0.25 to avoid small oscillations appearing when a larger time step is used.

In all of the examples considered in this section, the reaction is assumed to occur instantaneously, that is, $\varepsilon \approx 0$, and thus the value of ε does not need to be specified as it is not used in the direct projection (2.5). It should be observed that one can, in principle, set a very small value of ε and replace the direct projection (2.5) with solving the corresponding ODE (1.7). This, however, leads to almost identical results and therefore in the extremely stiff case we always use a simpler approach based on the direct projection. In Section 4.3, we will also demonstrate that the stiff case reduces to the extremely stiff case when $\varepsilon \to 0$.

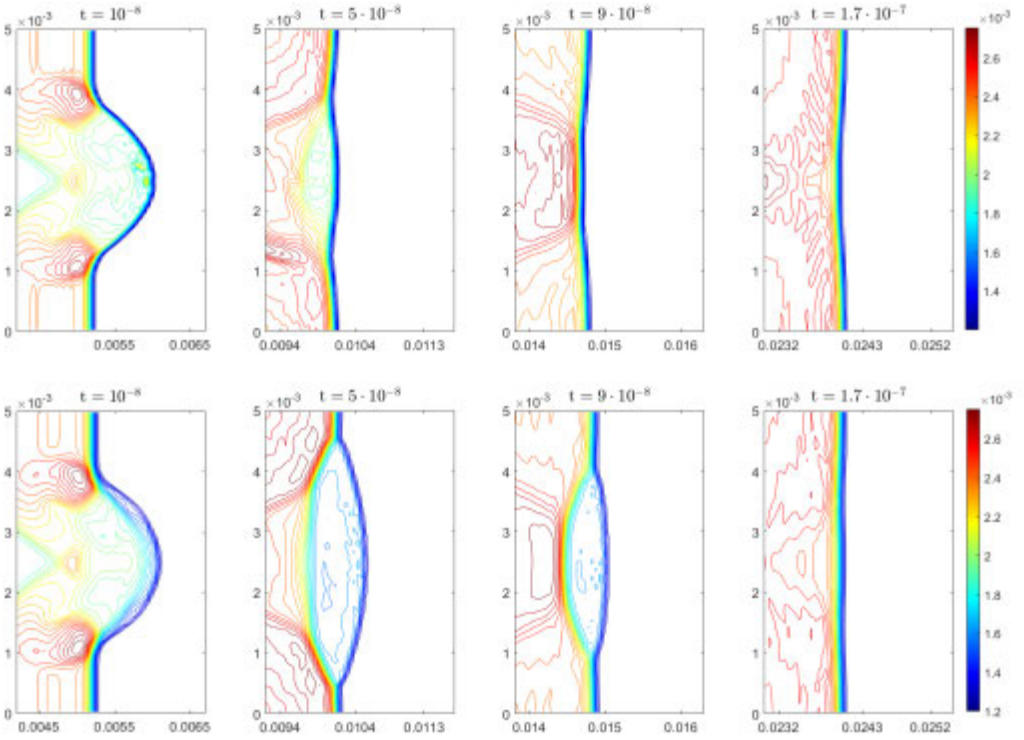

FIG. 2.1. *Example 1: Density ρ computed by the ADP (top row) and SDP (bottom row) methods.*

Example 1–detonation wave in a channel. We consider the initial-boundary value problem taken from [2]. The initial data,

$$(\rho(x,y,0),u(x,y,0),v(x,y,0),p(x,y,0),z(x,y,0)) = \begin{cases} (\rho_l,u_l,0,p_1,0), & \text{if } x \le \xi(y), \\ (\rho_r,u_r,0,p_r,1), & \text{if } x > \xi(y), \end{cases}$$

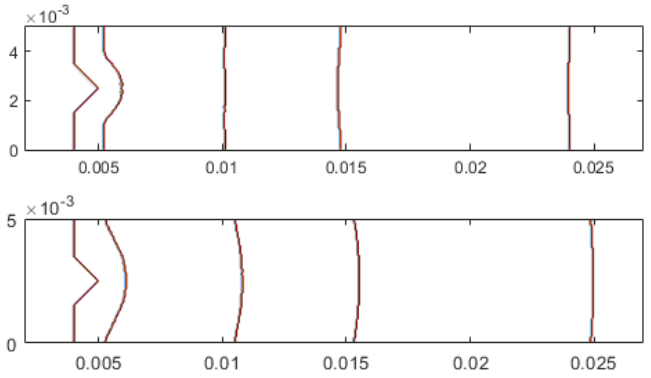

FIG. 2.2. *Example 1: Time evolution of the fraction of unburnt gas z computed by the ADP (top row) and SDP (bottom row) methods. In both figures, the detonation wave propagates from left to right and the interface between the burnt and unburnt fractions of the gas is shown at times $t=0$, 10^{-8}, $5\cdot10^{-8}$, $9\cdot10^{-8}$ and $1.7\cdot10^{-7}$.*

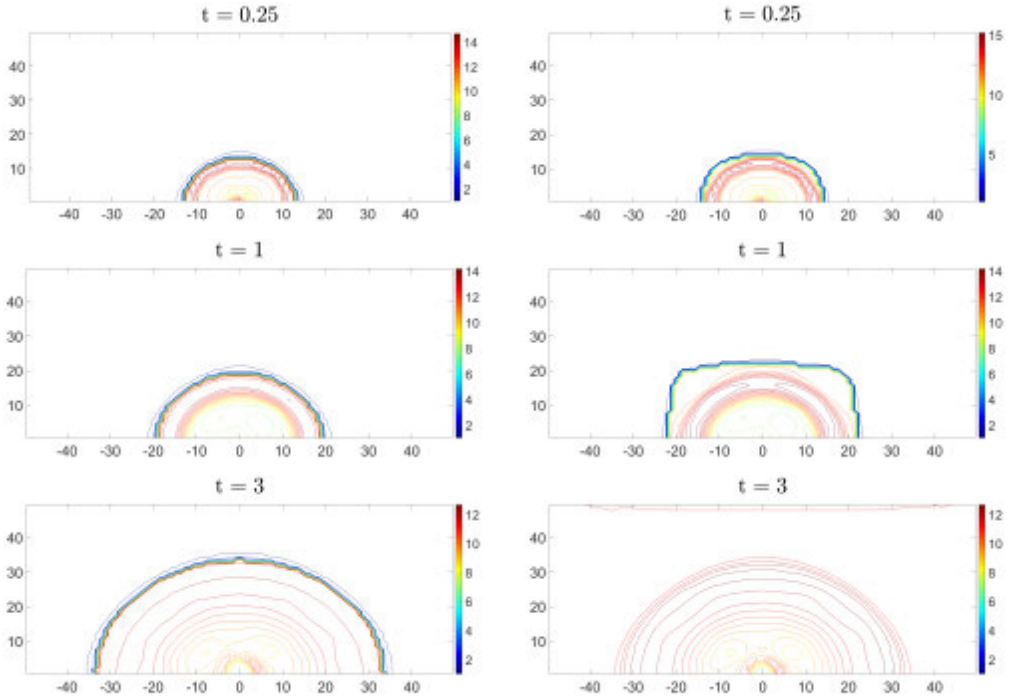

FIG. 2.3. *Example 2: Temperature τ computed by the ADP (left column) and SDP (right column) methods.*

where

$$\xi(y)=\begin{cases}0.004, & \text{if } |y-0.0025|\geq 0.001,\\ 0.005-|y-0.0025|, & \text{if } |y-0.0025|<0.001,\end{cases}$$

are given in a 2-D channel $[0,0.025]\times[0,0.005]$ with the solid wall boundary conditions at the upper and lower boundaries and free boundary conditions on the left and on

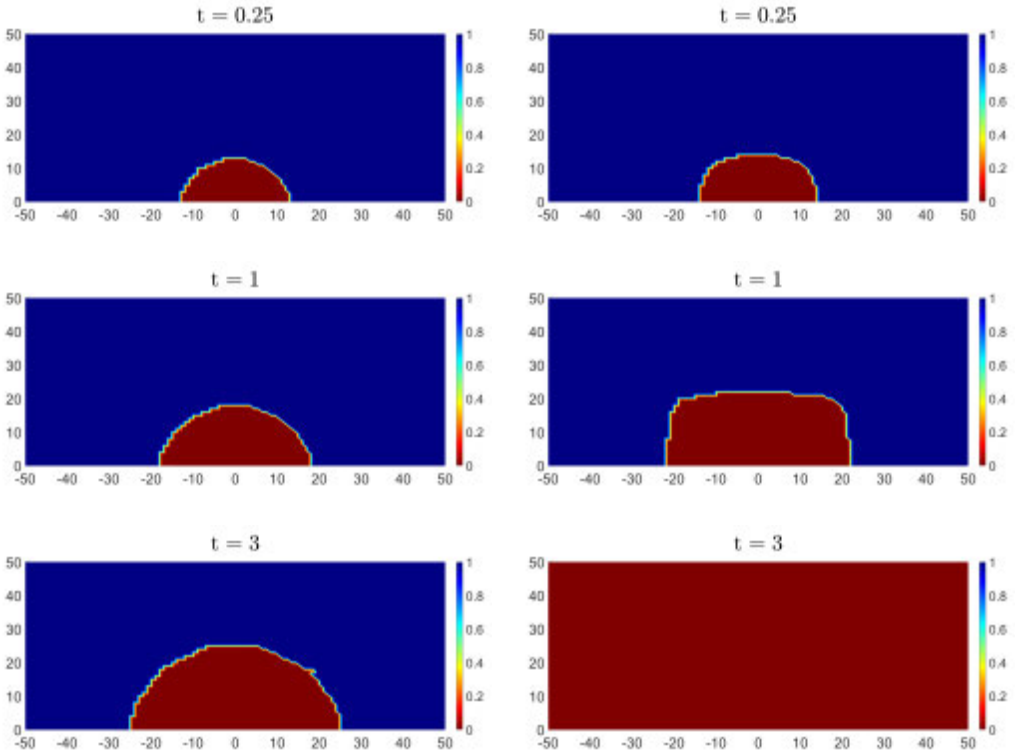

FIG. 2.4. *Example 2: Fraction of unburnt gas z (shaded in red) computed by the ADP (left column) and SDP (right column) methods.*

the right. We take the following parameter values: $\gamma = 1.4$, $q_0 = 5.196 \times 10^9$ and $\tau_c = 1.155 \times 10^9$, and the initial values: $\rho_l = 1.945 \times 10^{-3}$, $p_l = 6.27 \times 10^6$, $u_l = 8.162 \times 10^4$, $\rho_r = 1.201 \times 10^{-3}$, $p_r = 8.321 \times 10^5$ and $u_r = 0$, which are the same as in [2].

One important feature of this solution is that the triple points travel in the transverse direction and bounce back and forth against the upper and lower walls, forming a cellular pattern.

We compute the solutions by using both the ADP and SDP methods on a uniform spatial mesh with $\Delta x = \Delta y = 5 \times 10^{-5}$. In Figure 2.1, we show the density computed at four different times using the ADP (top row) and SDP (bottom row) methods. The ADP results are in good agreement with the results reported in [2], while the SDP solution develops a wave traveling with a nonphysical speed. This can also be clearly seen in Figure 2.2, where we show the propagation of the interface between the burnt and unburnt fractions of the gas, computed by the two studied methods.

Example 2–radial detonation wave. In the second example taken from [3], we consider the initial setting, which corresponds to a circular detonation front and consists of totally burnt gas inside a semi-circle with radius 10 and totally unburnt gas outside the semi-circle and the radially symmetric initial velocities. The radially symmetric initial data are

$$(\rho,u,v,p,z)(x,y,0) = \begin{cases} (\rho_{\text{in}}, u_{\text{in}}(x,y), v_{\text{in}}(x,y), p_{\text{in}}, 0), & \text{if } r \le 10, \\ (1,0,0,1,1), & \text{if } r > 10, \end{cases} \qquad r = \sqrt{x^2+y^2},$$

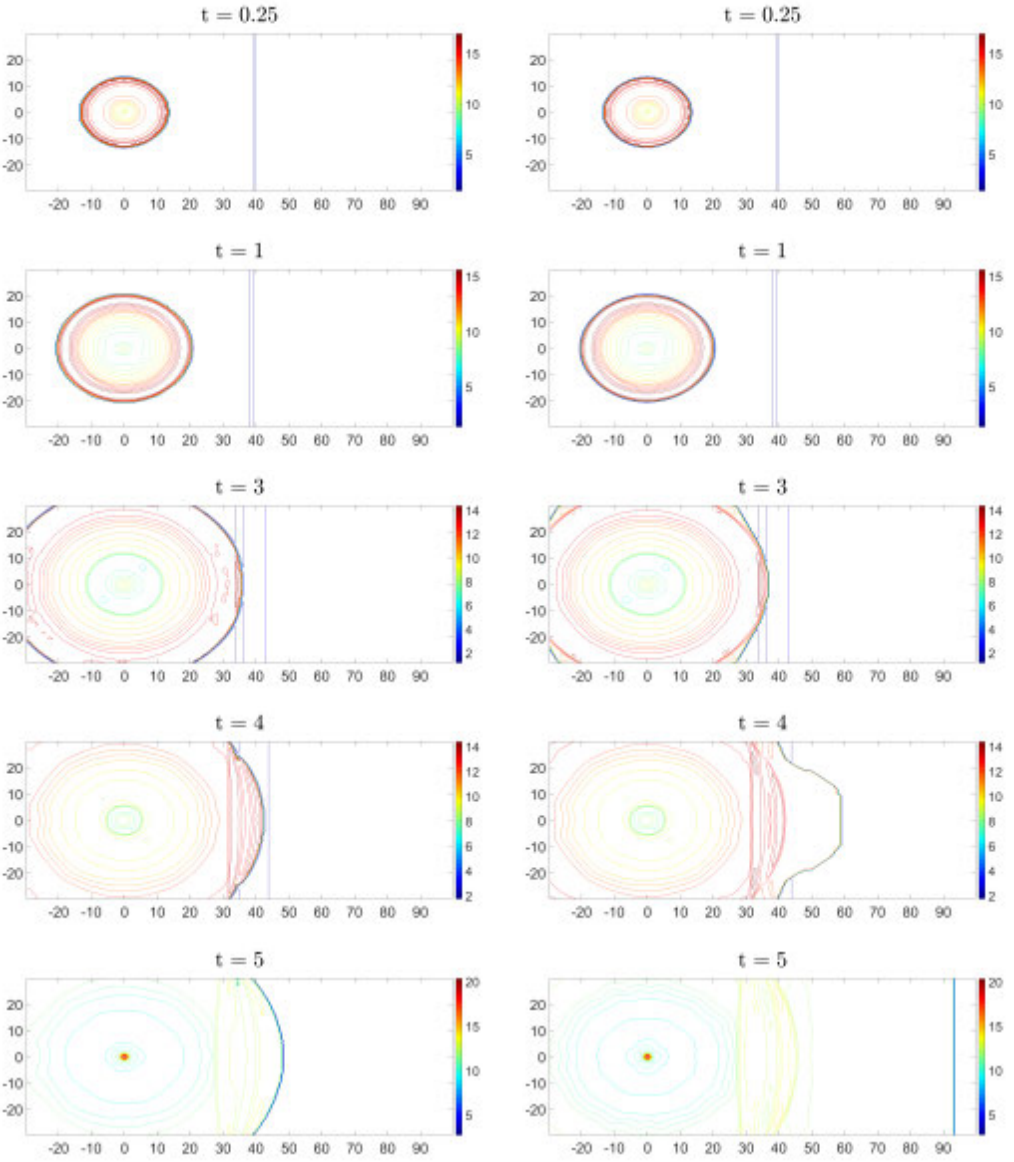

FIG. 2.5. *Example 3: Temperature τ computed by the ADP (left column) and SDP (right column) methods.*

where $p_{\text{in}} = 21.53134$, $\rho_{\text{in}} = 1.79463$, $u_{\text{in}}(x,y) = 10x/r$, and $v_{\text{in}}(x,y) = 10y/r$. The parameters are chosen as $\gamma = 1.2$, $q_0 = 50$ and $\tau_c = 2$.

We take the computational domain $[-50,50] \times [0,50]$ and use a uniform spatial mesh with $\Delta x = \Delta y = 1$. The solid wall boundary conditions are used along the bottom part of the domain, while the free boundary conditions are implemented at the other parts of the boundary. We have solved the problem numerically by both the ADP and SDP methods and the obtained results are reported in Figures 2.3 and 2.4.

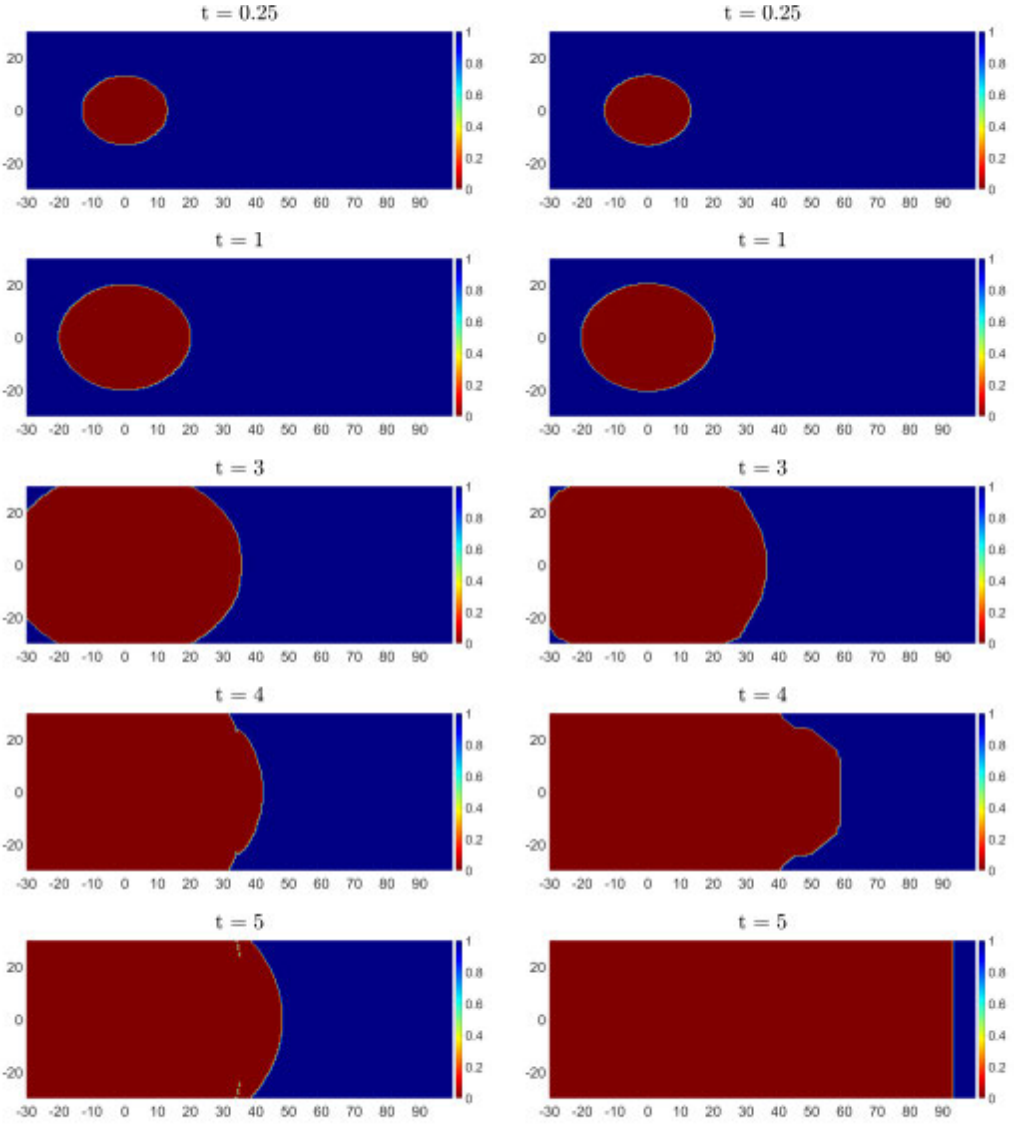

FIG. 2.6. *Example 3: Fraction of unburnt gas z (shaded in red) computed by the ADP (left column) and SDP (right column) methods.*

In Figure 2.3, we plot the temperature component of the computed solution at times $t = 0.25$, 1 and 3. As one can see, the ADP and SDP temperatures are totally different even at a smaller time $t = 0.25$. The source of this difference can be understood by looking at the propagation of the interface between the burnt and unburnt fractions of the gas shown in Figure 2.4. As the ADP solution is in a good agreement with the solution reported in [3], we conclude that the fast wave developed by the SDP solution is a numerical artifact that can be prevented by using the proposed ADP.

Example 3–interaction of gas dynamics and detonation waves. In the third example, we study the collision of a radially symmetric stiff detonation wave with a

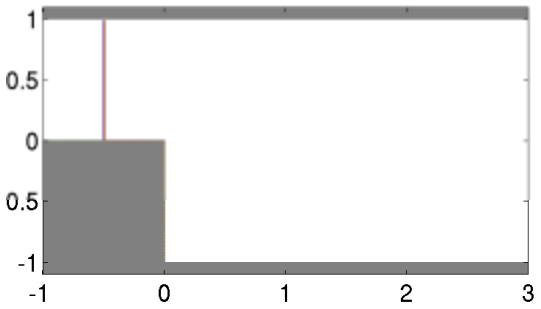

FIG. 2.7. *Example 4: Domain and the initial wave location.*

shock, contact discontinuity and rarefaction wave. This problem is an extension of the 1-D experiment conducted in [3, 15, 16]. We consider the following initial data:

$$(\rho,u,v,p,z)(x,y,0)=\begin{cases}(4,0,0,10,0), & \text{if } x>40,\\ (3.64282,10\cos\theta,10\sin\theta,54.8244,0), & \text{if } \sqrt{x^2+y^2}<10,\\ (1,0,0,1,1), & \text{otherwise,}\end{cases}$$

where $\tan\theta=y/x$ and use the following parameters: $\gamma=1.2$, $q_0=50$ and $\tau_c=3$. We take the computational domain $[-30,100]\times[-30,30]$, on which we implement free boundary conditions, and use a uniform spatial mesh with $\Delta x=\Delta y=1/2$.

The results (temperature and fraction of unburnt gas) obtained by the ADP and SDP methods at times $t=0.25$, 1, 3, 4 and 5 are reported in Figures 2.5 and 2.6. As one can observe, both methods provide similar approximations at small times $t=0.25$ and 1 (before the collision). At a later time $t=3$ (after the collision with the shock, but before the collision with the rarefaction wave), the solutions start exhibiting a different behavior due to the fact that the detonation wave produced by the SDP method starts moving with a nonphysical speed; this is similar to the 1-D case studied in [16]. Finally, at times $t=4$ and 5 (after all the collisions), the detonation wave front computed by the SDP method keeps moving to the right with the increasing nonphysical speed. At the same time, the ADP method seems to produce accurate results.

Example 4–diffraction of a detonation wave. In the last example of this section, we consider a detonation wave in the domain $[-1,0]\times[0,1]\cup[0,3]\times[-1,1]$ with the solid walls along the top part of the boundary and along the following line segments: $\{-1\le x\le 0, y=0\}$, $\{x=0,-1\le y\le 0\}$ and $\{0\le x\le 3, y=-1\}$, and the open boundaries on the left and on the right. The initial data are

$$(\rho,u,v,p,z)(x,y,0)=\begin{cases}(3.64282,6.2489,0,54.8244,0), & \text{if } x\le -0.5,\\ (1,0,0,1,1), & \text{if } x>-0.5,\end{cases}$$

and the parameters are the same as in Example 2: $\gamma=1.2$, $q_0=50$ and $\tau_c=2$. The initial setting is outlined in Figure 2.7.

In this example, the detonation wave initially positioned vertically at $x=-0.5$, first propagates to the right and then diffracts around a solid corner. We compute the solution at times $t=0.2$ and 0.4 on a uniform spatial grid with $\Delta x=\Delta y=1/100$ using both the ADP and SDP methods. The results are shown in Figures 2.8 and 2.9, where we plot the temperature and the fraction of unburnt gas fields. As one can clearly see, an artificially fast wave generated by the SDP method after the diffraction, is prevented by the use of the proposed ADP procedure.

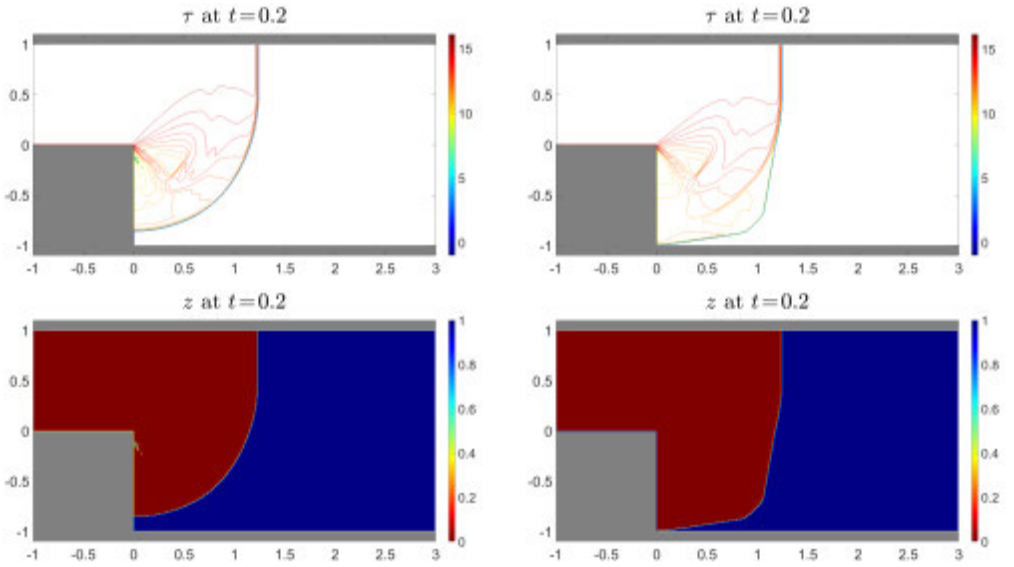

FIG. 2.8. *Example 4: Temperature τ (top row) and fraction of unburnt gas z (bottom row) at time $t=0.2$ computed by the ADP (left column) and SDP (right column) methods.*

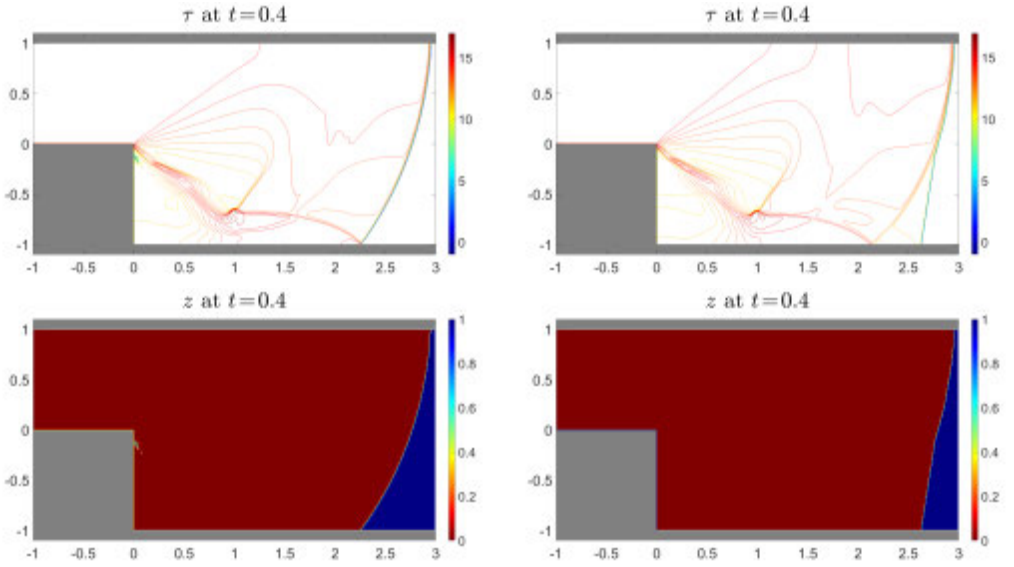

FIG. 2.9. *Example 4: Same as in Figure 2.8, but at time $t=0.4$.*

3. Accurate deterministic projection method: stiff case

We now consider a stiff, but not extremely stiff regime. In this case, instead of performing a direct projection (1.8) one has to numerically solve the stiff ODE (1.7) at the projection substep $S_{\mathcal{P}}$.

To do so, we first note that the last equation of the system (1.2) can be combined

with the density equation and then recast in the nonconservative form as

$$z_t + uz_x + vz_y = -zK(\tau;\varepsilon,\tau_c),$$

where $K(\tau;\varepsilon,\tau_c)$ is given by either (1.4) or (1.5). Therefore, at the projection substep $S_{\mathcal{P}}$, we will have to solve the following stiff ODEs at every cell center (x_j,y_k):

$$\frac{\mathrm{d}}{\mathrm{d}t}z_{j,k} = -z_{j,k}K\big(\tau_{j,k}^{n+1}(z);\varepsilon,\tau_c\big), \quad t\in[t^n,t^{n+1}). \tag{3.1}$$

We note that the RHS of (3.1) is prescribed upon the completion of the hydrodynamic substep $S_{\mathcal{H}}$ and thus it depends on $\tau_{j,k}^{n+1}(z)$, which is defined in (2.2), (2.3) and according to the ADP approach, remains constant on the time interval $[t^n,t^{n+1})$ as we do not update z until the projection substep $S_{\mathcal{P}}$ is completed. Therefore, $K\big(\tau_{j,k}^{n+1}(z);\varepsilon,\tau_c\big)$ also remains constant, that is, $K\big(\tau_{j,k}^{n+1}(z);\varepsilon,\tau_c\big)\equiv K\big(\tau_{j,k}^{n+1}(z_{j,k}^n);\varepsilon,\tau_c\big)$ for $t\in[t^n,t^{n+1})$, and we can solve the ODE (3.1) exactly to obtain

$$z_{j,k}^{n+1} = z_{j,k}^n\exp\Big\{-\Delta t\,K\big(\tau_{j,k}^{n+1}(z_{j,k}^n);\varepsilon,\tau_c\big)\Big\},$$

where $\tau_{j,k}^{n+1}(z_{j,k}^n)$ is calculated using (2.2), (2.3) with $z=z_{j,k}^n$.

Remark 3.1. We note that in the SDP method, $K\big(\tau_{j,k}^{n+1}(z);\varepsilon,\tau_c\big)$ is not constant for $t\in[t^n,t^{n+1})$ as we update z during the hydrodynamics substep $S_{\mathcal{H}}$. Therefore, in order to design the SDP method, we develop a proper ODE solver for (3.1). To this end, we first rewrite it in terms of an auxiliary variable $w:=\ln z$,

$$w_t = -K\big(\tau_{j,k}^{n+1}(z);\varepsilon,\tau_c\big), \tag{3.2}$$

and then apply the trapezoidal method to equation (3.2) and implement it in an explicit form using the predictor-corrector approach. This results in

$$w_{j,k}^{n+1} = w_{j,k}^* - \frac{\Delta t}{2}\Big[K\big(\tau_{j,k}^{n+1}(z_{j,k}^*);\varepsilon,\tau_c\big) + K\big(\tau_{j,k}^{n+1}(\tilde{z}_{j,k}^{n+1});\varepsilon,\tau_c\big)\Big],$$

where $\tilde{w}_{j,k}^{n+1}=\ln(\tilde{z}_{j,k}^{n+1})$ is the value predicted by the forward Euler method, namely,

$$\tilde{w}_{j,k}^{n+1} = w_{j,k}^* - \Delta t K\big(\tau_{j,k}^{n+1}(z_{j,k}^*);\varepsilon,\tau_c\big).$$

After the backward substitution $z=e^w$, we obtain the following trapezoidal-like ODE method to compute $z_{j,k}^{n+1}$:

$$z_{j,k}^{n+1} = z_{j,k}^*\exp\left\{-\frac{\Delta t}{2}\Big[K\big(\tau_{j,k}^{n+1}(z_{j,k}^*);\varepsilon,\tau_c\big) + K\big(\tau_{j,k}^{n+1}(\tilde{z}_{j,k}^{n+1});\varepsilon,\tau_c\big)\Big]\right\}$$

with

$$\tilde{z}_{j,k}^{n+1} = z_{j,k}^*\exp\Big\{-\Delta t K\big(\tau_{j,k}^{n+1}(z_{j,k}^*);\varepsilon,\tau_c\big)\Big\},$$

where $\tau_{j,k}^{n+1}(z_{j,k}^*)$ and $\tau_{j,k}^{n+1}(\tilde{z}_{j,k}^{n+1})$ are calculated using (2.2) and (2.3) with $z=z_{j,k}^*$ and $z=\tilde{z}_{j,k}^{n+1}$, respectively.

3.1. Numerical examples. In this section, we present three numerical experiments, in which we consider stiff, but not extremely stiff, 1-D and 2-D problems with the Arrhenius kinetic term (1.4). Notice that the 2-D ADP method proposed in Section 3 can be reduced to the 1-D case in a straightforward way. In all of the examples, the CFL number is set to 0.3.

Example 5—1-D detonation waves. We first consider the 1-D example taken from [28,33,38]. The initial conditions, which correspond to a burnt gas on the left and unburnt gas on the right, are given by

$$(\rho,u,p,z)(x,0)=\begin{cases}(1.6812,2.8867,21.5672,0), & \text{if } x\le 10,\\ (1,0,1,1), & \text{if } x>10,\end{cases}$$

and the parameters are chosen as $\gamma=1.4$, $q_0=25$, $1/\varepsilon=16418$ and $\tau_c=15$. We take the computational domain $[0,30]$ and use a uniform spatial mesh with $\Delta x=1/10$. The density, pressure, temperature and fraction of unburnt gas, computed by both the ADP and SDP methods at $t=1.5$, are presented in Figure 3.1 together with the reference solution obtained on a uniform spatial mesh with $\Delta x=3/4000$. It is important to point out that the reference solution cannot be computed with $\Delta x\gtrsim 1/200$ as the unsplit central-upwind scheme must be fully resolved (otherwise, it will suffer from the same drawback as the SDP method, that is, the computed detonation wave speed will become nonphysical). As one can see, the proposed ADP method captures the detonation wave propagating with the correct speed, while the detonation wave computed by the SDP method moves faster. Also note that our results are in good agreement with those reported in [38, Example 4.1].

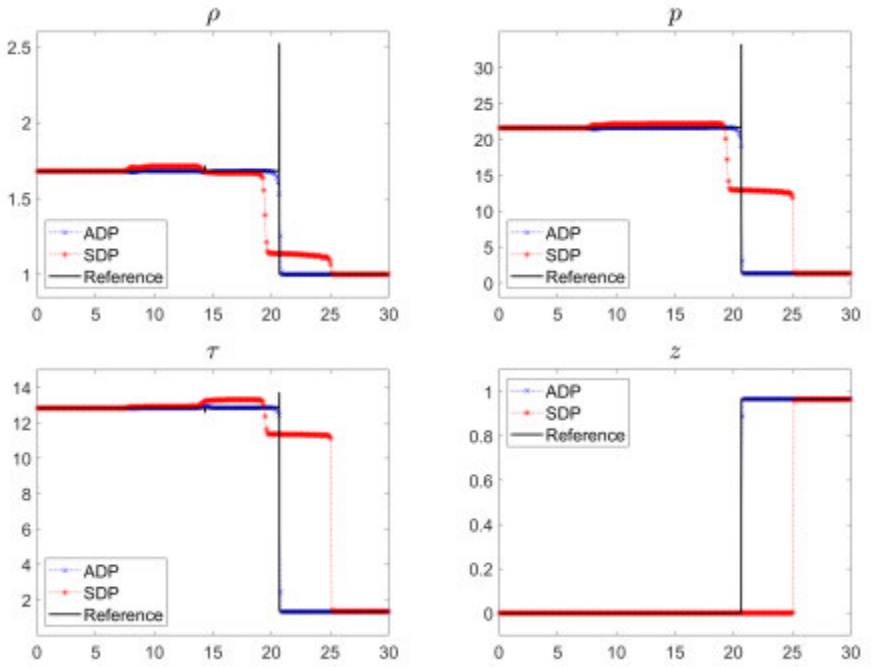

FIG. 3.1. *Example 5: Density (ρ), pressure (p), temperature (τ) and mass fraction (z) computed by the ADP and SDP methods.*

Example 6—2-D Detonation Waves. We now consider the 2-D example taken from [38], and take the initial conditions similar to those in Example 2, but put into the radially symmetric setting:

$$(\rho,u,v,p,z)(x,y,0)=\begin{cases}(\rho_{\rm in},u_{\rm in}(x,y),v_{\rm in}(x,y),p_{\rm in},0), & \text{if } r\le 2,\\ (1,0,0,1,1), & \text{if } r>2,\end{cases}$$

where $r=\sqrt{x^2+y^2}$, $p_{\rm in}=21.53134$, $\rho_{\rm in}=1.79463$, $u_{\rm in}(x,y)=10x/r$ and $v_{\rm in}(x,y)=10y/r$. The parameters are $\gamma=1.4$, $q_0=30$, $1/\varepsilon=20000$ and $\tau_c=15$. The computational domain is $[-10,10]\times[0,10]$ and we use a uniform mesh with $\Delta x=\Delta y=1/10$. We compute the solution using both the ADP and SDP methods until the final time $t=1$ and present the obtained density, pressure, temperature and fraction of unburnt gas along the $y=x$ 1-D cross-section in Figure 3.2. Unfortunately, no reference solution can be computed in the 2-D case as a fully resolved unsplit central-upwind scheme is computationally unaffordable. In order to verify that the ADP solution converges to the physically relevant one, we also plot the ADP and SDP solutions computed using a finer mesh with $\Delta x=\Delta y=1/40$. As one can see, the position of the detonation wave in the obtained ADP solutions is about the same, which suggests that the ADP method captures the detonation wave propagating with the correct speed. We would also like to point out that our results are similar to those reported in [38, Example 4.4].

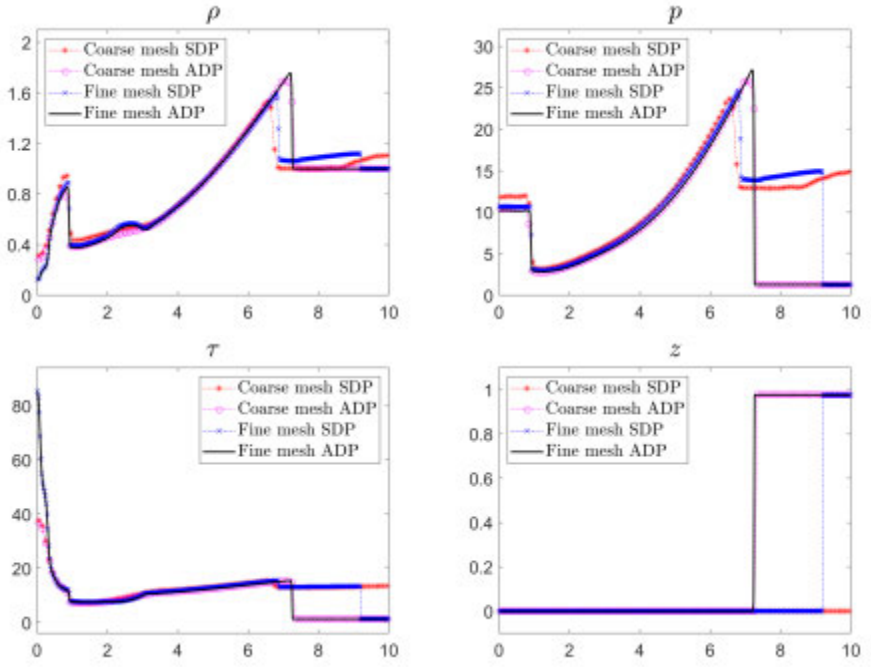

FIG. 3.2. *Example 6: 1-D cross-sections along the $y=x$ of the density (ρ), pressure (p), temperature (τ) and mass fraction (z) computed by the ADP and SDP methods using the coarse mesh with $\Delta x=\Delta y=1/10$ and a finer mesh with $\Delta x=\Delta y=1/40$.*

Example 7–diffraction of detonation waves. In this example designed in the spirit of the numerical experiments conducted in [1], we consider several stiff detonation

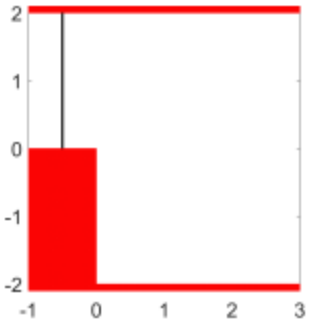

FIG. 3.3. *Example 7: Domain and the initial wave location.*

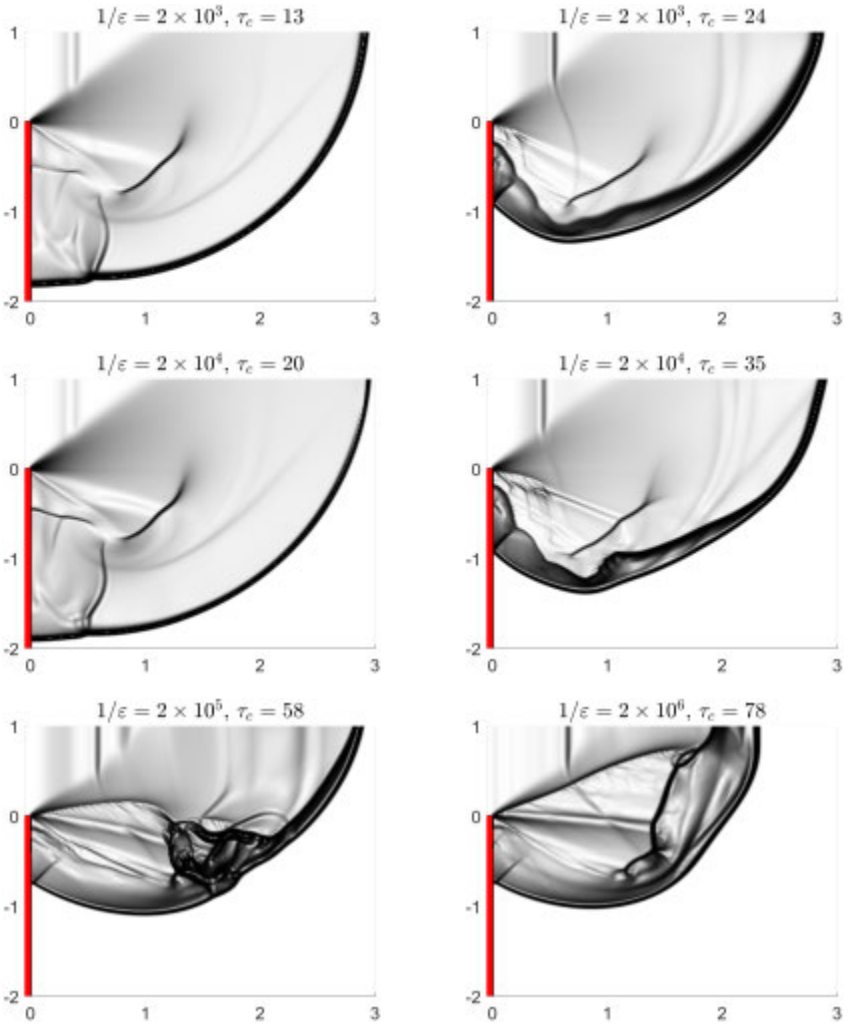

FIG. 3.4. *Example 7: Schlieren images of the magnitude of the density gradient field* $|\nabla\rho|$ *computed by the ADP method for different values of* ε *and* τ_c.

waves satisfying the same following initial data:

$$(\rho,u,v,p)(x,y,0)=\begin{cases}(3.64282,6.2489,0,54.8244,), & \text{if } x\le -0.5,\\ (1,0,0,1), & \text{if } x>-0.5.\end{cases}$$

The parameters $\gamma=1.2$ and $q_0=50$ are fixed, but the values of ε and τ_c are varied to model different regimes.

The initial setting is similar to the one used in Example 4 and it is outlined in Figure 3.3. The computational domain is $[-1,0]\times[0,2]\cup[0,3]\times[-2,2]$ and the solid walls boundary conditions are imposed along the top part of the boundary and along the following three line segments: $\{-1\le x\le 0, y=0\}$, $\{x=0,-2\le y\le 0\}$, and $\{0\le x\le 3, y=-2\}$, while the left and right boundaries are open.

We compute the solutions for six different combinations of parameters ε and τ_c on a uniform spatial grid with $\Delta x=\Delta y=1/100$. As in Example 4, the detonation waves initially situated vertically at $x=-0.5$, first travel to the right, and then diffract around a solid corner. The solutions obtained using the proposed ADP method at the final time $t=0.4$ are presented in Figure 3.4. As in [1], we plot Schlieren images of the magnitude of the density gradient field $|\nabla\rho|$. To this end, we have used the following shading function:

$$0.8\exp\left(-\frac{30|\nabla\rho|}{\max(|\nabla\rho|)}\right),$$

where the numerical density derivatives are computed using standard central differencing. As one can see from this figure, the solution structure dramatically changes when the reaction time is reduced and the ignition temperature increases. It is clear that small solution structures studied in [1] cannot be fully reproduced in underresolved simulations, but the main solution features can be captured by the ADP method.

4. ADP methods for multispecies detonation

In this section, we extend the ADP methods described in Section 2.2 and Section 3 to the multispecies detonation; see, e.g., [4,31,32,36–38].

The governing equations now read as (1.1) with

$$\boldsymbol{U}=\begin{pmatrix}\rho\\ \rho u\\ \rho v\\ E\\ \rho z_1\\ \vdots\\ \rho z_{N-1}\end{pmatrix},\ \boldsymbol{F}(\boldsymbol{U})=\begin{pmatrix}\rho u\\ \rho u^2+p\\ \rho uv\\ u(E+p)\\ \rho uz_1\\ \vdots\\ \rho uz_{N-1}\end{pmatrix},\ \boldsymbol{G}(\boldsymbol{U})=\begin{pmatrix}\rho v\\ \rho uv\\ \rho v^2+p\\ v(E+p)\\ \rho vz_1\\ \vdots\\ \rho vz_{N-1}\end{pmatrix},\ \boldsymbol{S}(\boldsymbol{U},\varepsilon)=\begin{pmatrix}0\\ 0\\ 0\\ 0\\ S_1(\boldsymbol{U},\varepsilon)\\ \vdots\\ S_{N-1}(\boldsymbol{U},\varepsilon)\end{pmatrix},\tag{4.1}$$

and they are completed with the following EOS:

$$p=(\gamma-1)\Big[E-\frac{\rho}{2}(u^2+v^2)-\sum_{i=1}^{N}q_i\rho z_i\Big],\tag{4.2}$$

and the algebraic relation

$$\sum_{i=1}^{N}z_i=1-z_{\text{cat}}.\tag{4.3}$$

In (4.1)–(4.3), $\boldsymbol{z}:=(z_1,\dots,z_N)^\top$ and $\boldsymbol{q}:=(q_1,\dots,q_N)^\top$ are the mass fractions and heat releases of the N chemical species, respectively, $z_{\rm cat}$ is the total mass fraction of the catalysts, $\boldsymbol{\varepsilon}:=(\varepsilon_1,\dots,\varepsilon_M)^\top$ are the parameters representing the reaction times of M reactions, and

$$S_i(\boldsymbol{U},\boldsymbol{\varepsilon})=W_i\sum_{\ell=1}^{M}(v''_{i\ell}-v'_{i\ell})K(\tau;\varepsilon_\ell,\tau_\ell)\prod_{j=1}^{N}\Big(\frac{\rho z_j}{W_j}\Big)^{v'_{j\ell}},\quad i=1,\dots,N-1. \tag{4.4}$$

Here, W_i is the molecular weight of the i-th chemical species, $v''_{i\ell}$ and $v'_{i\ell}$ are the stoichiometric coefficients for the i-th species appearing as a product and a reactant in the ℓ-th reaction, τ_ℓ is the parameter representing the ignition temperature for the ℓ-th reaction, and $K(\tau;\varepsilon_\ell,\tau_\ell)$ is either the Arrhenius,

$$K(\tau;\varepsilon_\ell,\tau_\ell)=\frac{1}{\varepsilon_\ell}e^{-\tau_\ell/\tau},$$

or Heaviside,

$$K(\tau;\varepsilon_\ell,\tau_\ell)=\frac{1}{\varepsilon_\ell}H(\tau-\tau_\ell)=\begin{cases}\dfrac{1}{\varepsilon_\ell}, & \text{if}\quad \tau\ge\tau_\ell,\\ 0, & \text{otherwise,}\end{cases} \tag{4.5}$$

kinetic term.

Example. To cite an example, we consider a reacting model consisting of $N=4$ species and $M=2$ reactions. Prototype reactions for such model are

$$H_2+O_2\to 2OH,\qquad 2OH+H_2\to 2H_2O, \tag{4.6}$$

with $\tau_1\le\tau_2$ and N_2 being a catalyst. In this case, $v'_{1,1}=v'_{2,1}=1$, $v'_{3,1}=v'_{4,1}$, $v'_{1,2}=1$, $v'_{3,2}=2$, $v'_{2,2}=v'_{4,2}=0$, $v''_{3,1}=2$, $v''_{1,1}=v''_{2,1}=v''_{4,1}=0$, $v''_{4,2}=2$, $v''_{1,2}=v''_{2,2}=v''_{3,2}=0$, and thus formula (4.4) reads as

$$\begin{aligned}
S_1&=W_1\Big[-K(\tau;\varepsilon_1,\tau_1)\Big(\frac{\rho z_1}{W_1}\Big)\Big(\frac{\rho z_2}{W_2}\Big)-K(\tau;\varepsilon_2,\tau_2)\Big(\frac{\rho z_1}{W_1}\Big)\Big(\frac{\rho z_3}{W_3}\Big)^2\Big],\\
S_2&=W_2\Big[-K(\tau;\varepsilon_1,\tau_1)\Big(\frac{\rho z_1}{W_1}\Big)\Big(\frac{\rho z_2}{W_2}\Big)\Big],\\
S_3&=W_3\Big[2K(\tau;\varepsilon_1,\tau_1)\Big(\frac{\rho z_1}{W_1}\Big)\Big(\frac{\rho z_2}{W_2}\Big)-2K(\tau;\varepsilon_2,\tau_2)\Big(\frac{\rho z_1}{W_1}\Big)\Big(\frac{\rho z_3}{W_3}\Big)^2\Big],
\end{aligned} \tag{4.7}$$

where z_1, z_2, and z_3 are the mass fractions of hydrogen (H_2), oxygen (O_2), and hydroxide (OH), respectively, and the corresponding molecular weights are $W_1=2$, $W_2=32$, and $W_3=17$.

Finally, $z_{\rm cat}$ is the constant mass fraction of nitrogen (N_2), which is the catalyst, and the mass fraction of water (H_2O) is obtained directly from (4.3):

$$z_4=1-z_1-z_2-z_3-z_{\rm cat}. \tag{4.8}$$

For the simplicity of presentation, in the remaining part of Section 4, we restrict our consideration to the reactions presented in the above example.

4.1. Extremely stiff case. We begin with the extremely stiff case, in which the multispecies extension of the ADP method is quite straightforward. As before, the time evolution of the computed solution from time $t=t^n$ to $t=t^{n+1}$ consists of two splitting substeps. We first solve the system (2.4) to obtain the cell averages $\overline{\rho}_{j,k}^{n+1}$, $(\overline{\rho u})_{j,k}^{n+1}$, $(\overline{\rho v})_{j,k}^{n+1}$ and $\overline{E}_{j,k}^{n+1}$ and use them and the EOS (4.2) to obtain $u_{j,k}^{n+1}$, $v_{j,k}^{n+1}$, $p_{j,k}^{n+1}(\boldsymbol{z}_{j,k}^n)$ and $\tau_{j,k}^{n+1}(\boldsymbol{z}_{j,k}^n)$, where

$$p_{j,k}^{n+1}(\boldsymbol{z})=(\gamma-1)\left[\overline{E}_{j,k}^{n+1}-\frac{\overline{\rho}_{j,k}^{n+1}}{2}\left((u_{j,k}^{n+1})^2+(v_{j,k}^{n+1})^2\right)-\sum_{i=1}^{5}q_i\overline{\rho}_{j,k}^{n+1}z_i\right] \tag{4.9}$$

and

$$\tau_{j,k}^{n+1}(\boldsymbol{z})=\frac{p_{j,k}^{n+1}(\boldsymbol{z})}{\overline{\rho}_{j,k}^{n+1}}. \tag{4.10}$$

We then generalize the ADP operator (2.5) to the multispecies case as follows:

$$(z_i)_{j,k}^{n+1}=\begin{cases} z_i^{HT}, \text{ if } \ \tau_{j,k}^{n+1}(\boldsymbol{z}_{j,k}^n)\ge\tau_2,\\ z_i^{IT}, \ \text{ if } \ \tau_2>\tau_{j,k}^{n+1}(\boldsymbol{z}_{j,k}^n)\ge\tau_1, \quad i=1,2,3.\\ z_i^{LT}, \ \text{ if } \ \tau_{j,k}^{n+1}(\boldsymbol{z}_{j,k}^n)<\tau_1, \end{cases} \tag{4.11}$$

Here, z_i^{LT}, z_i^{IT} and z_i^{HT} are the mass fractions of the i-th chemical species in the low, intermediate and high temperature regimes, respectively. We note that when the temperature is lower than τ_1, no reactions occur, while when the temperature is higher than τ_2, then both reactions have been completed. The value of z_i^{IT} depends on the quantities of the reactants in the mixture. For the sake of brevity, we will only consider the case in which there is more hydrogen than oxygen, that is, $z_1^{LT}\ge\frac{W_1}{W_2}z_2^{LT}$. The values of the mass fractions z_i^{IT} are then given by

$$z_1^{IT}=z_1^{LT}-\frac{W_1}{W_2}z_2^{LT}, \quad z_2^{IT}=0, \quad z_3^{IT}=\frac{2W_3}{W_2}z_2^{LT}.$$

Finally, we note that $(z_5)_{j,k}^{n+1}=(z_5)_{j,k}^0$ as the mass fraction of a catalyst remains constant during the entire reaction process, and $(z_4)_{j,k}^{n+1}=1-(z_1)_{j,k}^{n+1}-(z_2)_{j,k}^{n+1}-(z_3)_{j,k}^{n+1}-(z_5)_{j,k}^{n+1}$ from (4.3).

4.2. Stiff case. In order to complete the derivation of the ADP method in the stiff case, we need to develop an ODE solver for the system of ODEs

$$(z_i)_t=\frac{1}{\rho}S_i, \quad i=1,\ldots,N-1, \tag{4.12}$$

with S_i given by (4.7) (or (4.4) in the general case). This system is supposed to be solved upon the completion of the hydrodynamic substep $S_{\mathcal{H}}$.

Equations (4.12) can be simplified as follows. First, it can be easily verified that

$$\left(z_3+\frac{2W_3}{W_1}z_1-\frac{4W_3}{W_2}z_2\right)_t=0,$$

which implies that the quantity

$$c:=z_3+\frac{2W_3}{W_1}z_1-\frac{4W_3}{W_2}z_2 \tag{4.13}$$

is independent of time. Therefore, z_3 can be obtained from (4.13) and substituted into (4.12) so that at the projection step $S_{\mathcal{P}}$ we will only need to solve a 2×2 system of ODEs consisting of the first two equations of (4.12) prescribed at every cell center (x_j,y_k). We then divide the first two equations of (4.12) by z_1 and z_2, respectively, introduce $w_1:=\ln z_1$ and $w_2:=\ln z_2$, and obtain the system

$$\frac{\mathrm{d}}{\mathrm{d}t}(w_1)_{j,k}=R_1(\boldsymbol{z}_{j,k}),\quad \frac{\mathrm{d}}{\mathrm{d}t}(w_2)_{j,k}=R_2(\boldsymbol{z}_{j,k}),\quad t\in[t^n,t^{n+1}), \tag{4.14}$$

with

$$R_1(\boldsymbol{z}_{j,k})=-\left[K_1\frac{\overline{\rho}^{n+1}_{j,k}(z_2)_{j,k}}{W_2}+K_2\left(\frac{\overline{\rho}^{n+1}_{j,k}(z_3)_{j,k}}{W_3}\right)^2\right],\quad R_2(\boldsymbol{z}_{j,k})=-K_1\frac{\overline{\rho}^{n+1}_{j,k}(z_1)_{j,k}}{W_1}, \tag{4.15}$$

$$(z_3)_{j,k}=c-\frac{2W_3}{W_1}(z_1)_{j,k}+\frac{4W_3}{W_2}(z_2)_{j,k}, \tag{4.16}$$

where $K_1:=K\big(\tau^{n+1}_{j,k}(\boldsymbol{z}^n_{j,k});\varepsilon_1,\tau_1\big)$ and $K_2:=K\big(\tau^{n+1}_{j,k}(\boldsymbol{z}^n_{j,k});\varepsilon_2,\tau_2\big)$ are constants for $t\in[t^{n+1},t^n)$ since in the ADP approach we compute the temperature based on the values of $\boldsymbol{z}$ from the time level $t=t^n$, and $\tau^{n+1}_{j,k}(\boldsymbol{z}^n_{j,k})$ is calculated using (4.9), (4.10) with $\boldsymbol{z}=\boldsymbol{z}^n_{j,k}$.

We solve the ODE system (4.14)–(4.16) in a predictor-corrector manner. First, we predict the solution at time $t=t^{n+1}$ using the forward Euler method, which in terms of $z_1=e^{w_1}$ and $z_2=e^{w_2}$ reads as

$$(\tilde{z}_1)^{n+1}_{j,k}=(z_1)^n_{j,k}\exp\big\{\Delta t R_1(\boldsymbol{z}^n_{j,k})\big\},\quad (\tilde{z}_2)^{n+1}_{j,k}=(z_2)^n_{j,k}\exp\big\{\Delta t R_2(\boldsymbol{z}^n_{j,k})\big\}. \tag{4.17}$$

The values of z_3 are then updated using (4.13):

$$(\tilde{z}_3)^{n+1}_{j,k}=c_{j,k}-\frac{2W_3}{W_1}(\tilde{z}_1)^{n+1}_{j,k}+\frac{4W_3}{W_2}(\tilde{z}_2)^{n+1}_{j,k},$$

where the time-independent quantities $c_{j,k}$ are given by

$$c_{j,k}=(z_3)^0_{j,k}+\frac{2W_3}{W_1}(z_1)^0_{j,k}-\frac{4W_3}{W_2}(z_2)^0_{j,k}, \tag{4.18}$$

the values of z_4 are obtained from (4.8):

$$(\tilde{z}_4)^{n+1}_{j,k}=1-(\tilde{z}_1)^{n+1}_{j,k}-(\tilde{z}_2)^{n+1}_{j,k}-(\tilde{z}_3)^{n+1}_{j,k}-(\tilde{z}_5)^{n+1}_{j,k},$$

and the values of z_5 remain unchanged, namely, $(\tilde{z}_5)^{n+1}_{j,k}=(z_5)^0_{j,k}$.

The computed values $(\tilde{z}_1)^{n+1}_{j,k}$ and $(\tilde{z}_2)^{n+1}_{j,k}$ are then updated with the help of a trapezoidal corrector, once again applied to the ODEs (4.14)–(4.16) and then written in terms of $z_1=e^{w_1}$ and $z_2=e^{w_2}$ as

$$\begin{aligned}(z_1)^{n+1}_{j,k}&=(z_1)^n_{j,k}\exp\left\{\frac{\Delta t}{2}\Big[R_1(\boldsymbol{z}^n_{j,k})+R_1(\tilde{\boldsymbol{z}}^{n+1}_{j,k})\Big]\right\},\\ (z_2)^{n+1}_{j,k}&=(z_2)^n_{j,k}\exp\left\{\frac{\Delta t}{2}\Big[R_2(\boldsymbol{z}^n_{j,k})+R_2(\tilde{\boldsymbol{z}}^{n+1}_{j,k})\Big]\right\}.\end{aligned} \tag{4.19}$$

Finally, the new values of z_3 are obtained using (4.13):

$$(z_3)^{n+1}_{j,k}=c_{j,k}-\frac{2W_3}{W_1}(z_1)^{n+1}_{j,k}+\frac{4W_3}{W_2}(z_2)^{n+1}_{j,k},$$

where $c_{j,k}$ are given in (4.18), the new values of z_4 are obtained from (4.8):

$$(z_4)_{j,k}^{n+1}=1-(z_1)_{j,k}^{n+1}-(z_2)_{j,k}^{n+1}-(z_3)_{j,k}^{n+1}-(z_5)_{j,k}^{n+1},$$

and the values of z_5 remain unchanged, namely, $(z_5)_{j,k}^{n+1}=(z_5)_{j,k}^{0}$.

REMARK 4.1. We note that in the SDP method, neither $K\big(\tau_{j,k}^{n+1}(\boldsymbol{z});\varepsilon_1,\tau_1\big)$ nor $K\big(\tau_{j,k}^{n+1}(\boldsymbol{z});\varepsilon_2,\tau_2\big)$ is constant for $t\in[t^{n+1},t^n)$ as we update $\boldsymbol{z}$ during the hydrodynamic substep $S_{\mathcal{H}}$. Therefore, when the SDP method is implemented, R_1 and R_2 in (4.15) are replaced with

$$\widehat{R}_1(\boldsymbol{z}_{j,k})=-\left[K\big(\tau_{j,k}^{n+1}(\boldsymbol{z});\varepsilon_1,\tau_1\big)\frac{\overline{\rho}_{j,k}^{n+1}(z_2)_{j,k}}{W_2}+K\big(\tau_{j,k}^{n+1}(\boldsymbol{z});\varepsilon_2,\tau_2\big)\left(\frac{\overline{\rho}_{j,k}^{n+1}(z_3)_{j,k}}{W_3}\right)^2\right],$$

$$\widehat{R}_2(\boldsymbol{z}_{j,k})=-K\big(\tau_{j,k}^{n+1}(\boldsymbol{z});\varepsilon_1,\tau_1\big)\frac{\overline{\rho}_{j,k}^{n+1}(z_1)_{j,k}}{W_1},$$

and (4.17) and (4.19) become

$$(\tilde{z}_1)_{j,k}^{n+1}=(z_1)_{j,k}^{*}\exp\Big\{\Delta t\widehat{R}_1(\boldsymbol{z}_{j,k}^{*})\Big\},\quad (\tilde{z}_2)_{j,k}^{n+1}=(z_2)_{j,k}^{*}\exp\Big\{\Delta t\widehat{R}_2(\boldsymbol{z}_{j,k}^{*})\Big\},$$

and

$$(z_1)_{j,k}^{n+1}=(z_1)_{j,k}^{*}\exp\left\{\frac{\Delta t}{2}\Big[\widehat{R}_1(\boldsymbol{z}_{j,k}^{*})+\widehat{R}_1(\tilde{\boldsymbol{z}}_{j,k}^{n+1})\Big]\right\},$$

$$(z_2)_{j,k}^{n+1}=(z_2)_{j,k}^{*}\exp\left\{\frac{\Delta t}{2}\Big[\widehat{R}_2(\boldsymbol{z}_{j,k}^{*})+\widehat{R}_2(\tilde{\boldsymbol{z}}_{j,k}^{n+1})\Big]\right\},$$

respectively.

4.3. Numerical examples. In order to illustrate the performance of the ADP methods for multispecies detonation, we conduct several numerical experiments in both 1-D and 2-D cases. As in Section 3.1, the 2-D ADP methods proposed in Section 4.1 and Section 4.2 can be reduced to their corresponding 1-D versions in a straightforward manner. In all of the numerical examples below, the Heaviside kinetic term (4.5) is used and the CFL value is chosen to be 0.3, except for Example 8a, where a smaller CFL value of 0.1 is used to reduce the numerical oscillations.

Example 8–one reaction. We begin with a multispecies case with one reaction

$$\mathrm{CH_4}+2\mathrm{O_2}\to\mathrm{CO_2}+2\mathrm{H_2O},$$

also studied in [4]. Here, $M=1$, $N=4$, $W_1=16$, $W_2=32$, $W_3=44$, $W_4=18$, $v'_{1,1}=1$, $v'_{2,1}=2$, $v'_{3,1}=0$, $v'_{4,1}=0$, $v''_{1,1}=0$, $v''_{2,1}=0$, $v''_{3,1}=1$ and $v''_{4,1}=2$, and formula (4.4) reads as

$$S_1=-\frac{1}{1024}K(\tau;\varepsilon_1,\tau_1)(\rho z_1)(\rho z_2)^2,\quad S_2=4S_1,\quad S_3=-\frac{11}{4}S_1,\tag{4.20}$$

where z_i, $i=1,2,3,4$ are the mass fractions of methane (CH_4), oxygen (O_2), carbon dioxide (CO_2), and water (H_2O), respectively.

Note that it is unnecessary to compute the source term S_4, since z_4 can be obtained directly from (4.3) and it is equal to $z_4=1-z_1-z_2-z_3$. We note that in the stiff case considered in Examples 8b and 8c, one only needs to compute S_1 since (4.20) immediately implies that $(z_2)_t-4(z_1)_t=0$ and $(z_3)_t+\frac{11}{4}(z_1)_t=0$. In Examples 8a–8c, we use the same parameters as in [4]: $\gamma=1.4$, $q_2=0$, $q_3=0$, $q_4=0$, $\tau_1=2$ and $q_1=500$ (in Examples 8a and 8b) or $q_1=100$ (in Example 8c).

Example 8a–1-D extremely stiff case. We begin with a 1-D extremely stiff case. The initial data are given by

$$(\rho,u,p,z_1,z_2,z_3,z_4)(x,0)=\begin{cases}(2,10,40,0,0.2,0.475,0.325), & \text{if } x\le 2.5,\\ (1,0,1,0.1,0.6,0.2,0.1), & \text{if } x>2.5.\end{cases} \tag{4.21}$$

In this example, we use the following ADP operator:

$$(z_i)_j^{n+1}=\begin{cases} z_i^{HT}, \text{ if } \tau_j^{n+1}(\boldsymbol{z}_j^n)\ge\tau_1,\\ z_i^{LT}, \text{ if } \tau_j^{n+1}(\boldsymbol{z}_j^n)<\tau_1,\end{cases}\quad i=1,2,3, \tag{4.22}$$

with $z_1^{HT}=0$, $z_1^{LT}=0.1$, $z_2^{HT}=0.2$, $z_2^{LT}=0.6$, $z_3^{HT}=0.475$, $z_3^{LT}=0.2$, and $(z_4)_j^{n+1}=1-(z_1)_j^{n+1}-(z_2)_j^{n+1}-(z_3)_j^{n+1}$. Here, $(\cdot)_j^{n+1}$ denotes the value of the corresponding variable in the 1-D cell C_j at time level $t=t^{n+1}$. We compute the numerical solution using both the ADP and SDP methods on the domain $[0,50]$ using uniform meshes with $\Delta x=1/4$ and $\Delta x=1/16$ until the final time $t=3$. The numerical results (density, pressure, temperature and mass fractions of CH_4) are presented in Figure 4.1. As one can observe, the solution consists of a detonation wave followed by a contact discontinuity and a shock, and they all seem to be accurately captured by the ADP method as the ADP results are in good agreement with those reported in [4, Example 5.3], while the solution computed by the SDP method is incorrect.

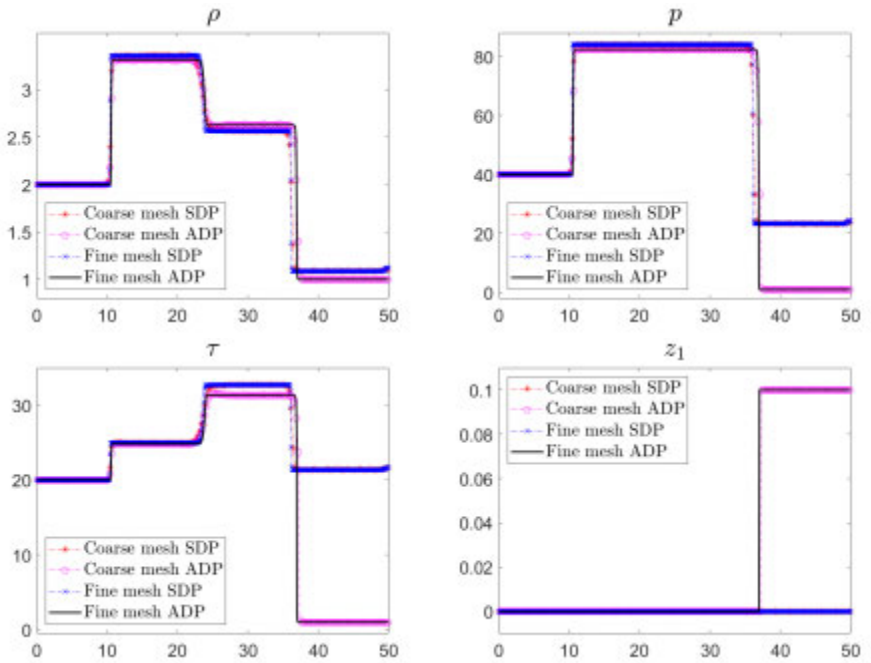

FIG. 4.1. *Example 8a: Density (ρ), pressure (p), temperature (τ) and mass fraction of* CH_4 *(z_1) computed by the ADP and SDP methods using the coarse mesh with $\Delta x=1/4$ and a finer mesh with $\Delta x=1/16$.*

Example 8b–1-D stiff case. We now turn our attention to the stiff case, in which we numerically integrate the ODE for z_1 (using the ODE solver similar to the

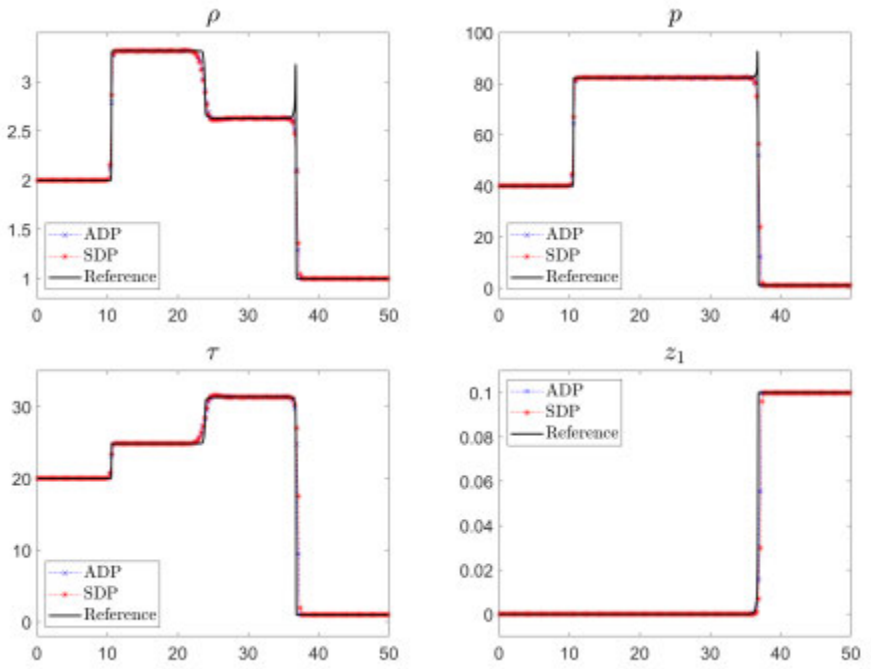

FIG. 4.2. *Example 8b: Density (ρ), pressure (p), temperature (τ) and mass fraction of* CH_4 *(z_1) computed by the ADP and SDP methods for* $1/\varepsilon_1 = 2\times 10^5$.

one described in Section 4.2) instead of applying the ADP operator (4.22). We use the same initial conditions (4.21) as in Example 8a.

We first take the value $1/\varepsilon_1 = 2\times 10^5$ used in [4] and compute the solutions by both ADP and SDP methods on the domain $[0,50]$ using a uniform mesh with $\Delta x = 1/4$ until the final time $t = 3$. The obtained results (density, pressure, temperature and mass fraction of CH_4) are presented in Figure 4.2 along with the reference solution, which is computed by the fully resolved unsplit central-upwind scheme using a very fine uniform mesh with $\Delta x = 1/100$. As one can see, both the ADP and SDP results are in good agreement with the reference solution computed on a mesh, which is sufficient to resolve the detonation wave structure—not only its accurate location. We also note that the unsplit central-upwind scheme fails to capture accurate detonation wave dynamics when $\Delta x \gtrsim 1/10$. However, the unsplit method still can be used in this case without being extremely inefficient. Therefore, we conclude that the value $1/\varepsilon_1 = 2\times 10^5$ corresponds to a stiff, but not extremely stiff case.

We then take the 10 times larger value of $1/\varepsilon_1 = 2\times 10^6$, repeat the same computations, and plot the obtained results in Figure 4.3. This time, the ADP and SDP solutions have been computed on the same uniform mesh with $\Delta x = 1/4$, but the fully resolved reference solution is obtained on a much finer (compared with the $1/\varepsilon_1 = 2\times 10^5$ case) mesh with $\Delta x = 1/1000$. Once again, the ADP is capable of exactly capturing the propagation of the detonation wave, while the SDP method fails. We also notice that in this case the unsplit central-upwind scheme fails if $\Delta x \gtrsim 1/100$, which brings us to the conclusion that the value $1/\varepsilon_1 = 2\times 10^6$ seems to correspond to the extremely stiff regime. In order to verify this, we plot, in Figure 4.3, the obtained solutions along

with the extremely stiff ADP solution computed using the ADP operator (4.22), that is, the ADP solution obtained in Example 8a. As one can see, the two ADP solutions are almost the same. This suggests that the extremely stiff case can be accurately treated using the stiff approach, that is, by using the ODE solver rather than the direct projection.

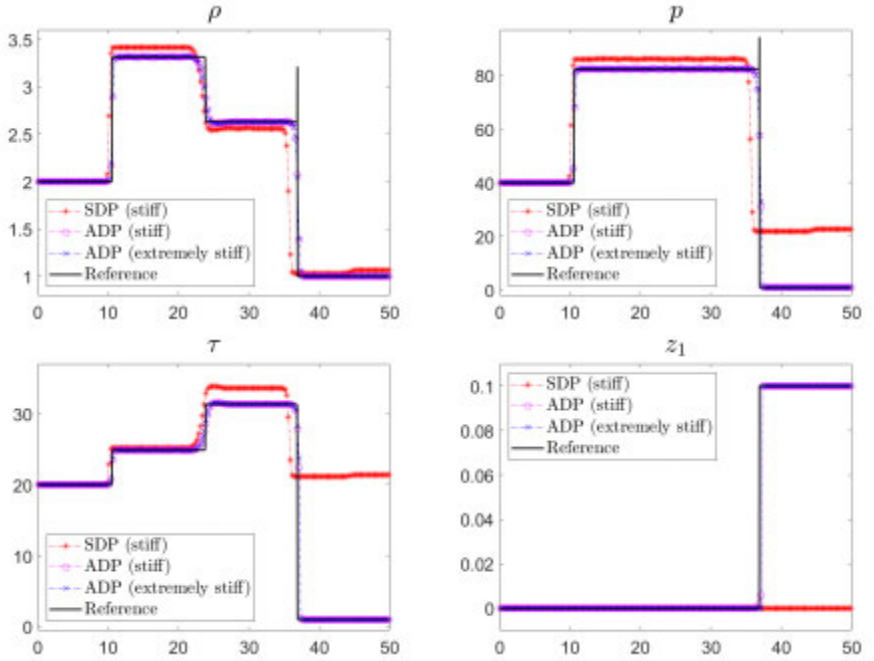

FIG. 4.3. *Example 8b: Density (ρ), pressure (p), temperature (τ) and mass fraction of CH_4 (z_1) computed by the stiff and extremely stiff ADP methods and the stiff SDP method for $1/\varepsilon_1 = 2\times 10^6$.*

Example 8c–2-D case. We now consider the 2-D case with the radially symmetric initial data

$$(\rho,u,v,p,z_1,z_2,z_3,z_4)(x,y,0) = \begin{cases} (2,u_{\text{in}}(x,y),v_{\text{in}}(x,y),40,0,0.2,0.475,0.325), & \text{if } r\le 10,\\ (1,0,0,1,0.1,0.6,0.2,0.1), & \text{if } r>10, \end{cases}$$

where $r=\sqrt{x^2+y^2}$, $u_{\text{in}}(x,y)=10x/r$ and $v_{\text{in}}(x,y)=10y/r$. As in Example 8a, the ADP operator is given by

$$(z_i)_{j,k}^{n+1} = \begin{cases} z_i^{HT}, \text{ if } \tau_{j,k}^{n+1}\ge \tau_1,\\ z_i^{LT}, \text{ if } \tau_{j,k}^{n+1}< \tau_1, \end{cases} \qquad i=1,2,3$$

with $z_1^{HT}=0$, $z_1^{LT}=0.1$, $z_2^{HT}=0.2$, $z_2^{LT}=0.6$, $z_3^{HT}=0.475$, $z_3^{LT}=0.2$, and $(z_4)_{j,k}^{n+1} = 1-(z_1)_{j,k}^{n+1}-(z_2)_{j,k}^{n+1}-(z_3)_{j,k}^{n+1}$. We solve this problem on the domain $[0,50]\times[0,50]$ using a uniform mesh with $\Delta x=\Delta y=1/4$. Solid wall boundary conditions are imposed along $x=0$ and $y=0$, while the free boundary conditions are used along the other parts of the boundary.

We consider both the extremely stiff ($1/\varepsilon_1=2\times 10^6$) and stiff ($1/\varepsilon_1=2\times 10^5$) cases and compute the numerical solutions by the extremely stiff and stiff ADP methods,

respectively. Figure 4.4 shows the pressure, temperature and mass fraction of CH_4 (we plot $100z_1$ rather then z_1 for a better visualization) along the line $y=x$, $x\geq 0$ at times $t=1$, 2, 4 and 6. As one can see, the extremely stiff and stiff results are almost the same and they are in good agreement with those reported in [4, Example 5.5]. We note that in this example, the SDP method yields quite accurate results (very close to those shown in Figure 4.4), which are omitted for the sake of brevity.

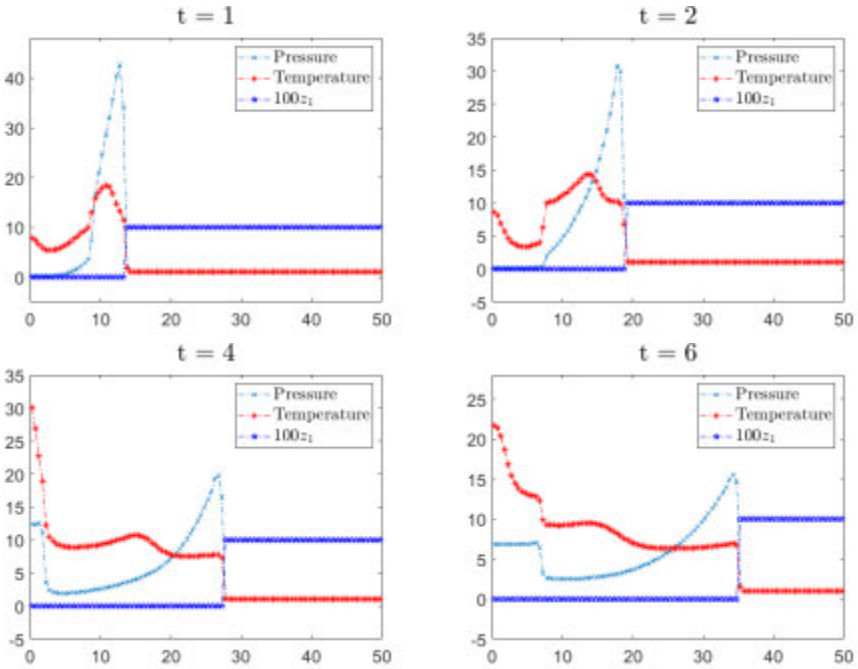

FIG. 4.4. *Example 8c: Pressure (p), temperature (τ) and 100 times of mass fraction of CH_4 ($100z_1$) computed by the ADP method at different times.*

Example 9–two reactions. In this example taken from [4, 37], we simulate the two reaction–five species model (4.1)–(4.2) for the reactions (4.6). The details of the model as well as the corresponding ADP methods are described and studied in Section 4. In Examples 9a–9d, we use the following parameters: $\gamma=1.4$, $q_1=0$, $q_2=0$, $q_4=-100$, $q_5=0$. Other parameters vary and will be specified in each particular example.

Example 9a–1-D extremely stiff case. We begin with the 1-D extremely stiff case studied subject to the following Riemann initial data also used in [4, Example 5.4]:

$$(\rho,u,p,z_1,z_2,z_3,z_4,z_5)(x,0)=\begin{cases}(2,10,40,0,0,0.17,0.63,0.2), & \text{if } x\leq 2.5,\\ (1,0,1,0.08,0.72,0,0,0.2), & \text{if } x>2.5.\end{cases}$$

In this example, we set $q_3=-20$ and use the 1-D version of the ADP operator (4.11) with $z_1^{HT}=0$, $z_1^{IT}=0.035$, $z_1^{LT}=0.08$, $z_2^{HT}=0$, $z_2^{IT}=0$, $z_2^{LT}=0.72$, $z_3^{HT}=0.17$, $z_3^{IT}=0.765$ and $z_3^{LT}=0$. We first compute the numerical solution with $\tau_1=2$ and $\tau_2=10$ (which were used in [4, Example 5.4]) by both the ADP and SDP methods in the computational domain $[0,50]$ using a uniform mesh with $\Delta x=1/4$ until the final time $t=3$. The numerical results (density, pressure, temperature and mass fractions of H_2) are presented

in Figure 4.5. As one can observe, the results computed by the ADP and SDP methods are practically the same and are in good agreement with those reported in [4, Example 5.4], except that the density and temperature fields plotted in [4, Figure 4] are smeared (this causes the pressure graph to be nonflat in the area $x \in [20,30]$) compared with much sharper jumps in ρ and τ and flat p around $x \in [20,30]$; seen in Figure 4.5.

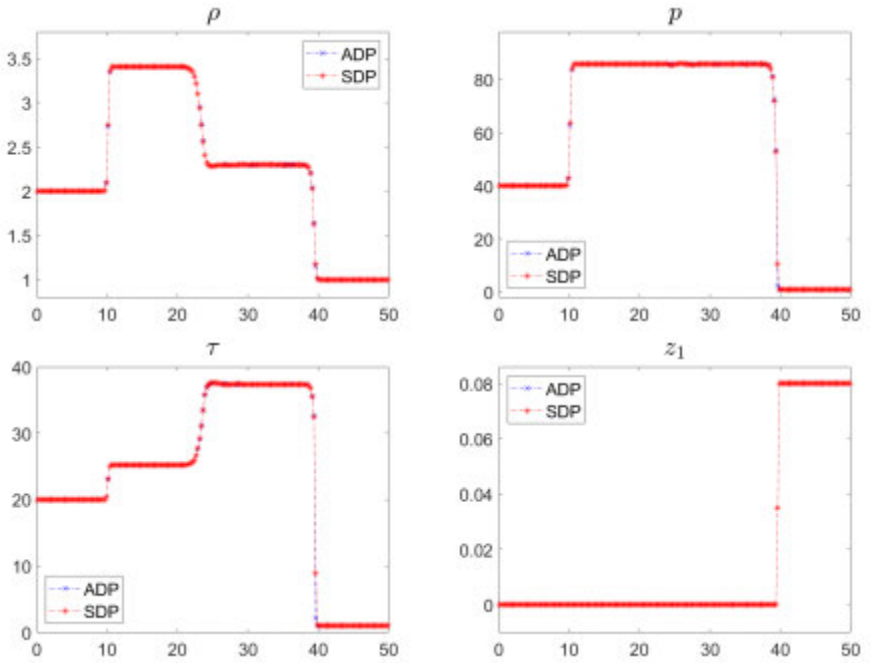

FIG. 4.5. *Example 9a: Density (ρ), pressure (p), temperature (τ) and mass fraction of* H_2 *(z_1) computed by the ADP and SDP methods for* $\tau_1 = 2$ *and* $\tau_2 = 10$.

We then consider more challenging, smaller values of the ignition temperature and take $\tau_1 = 1.5$ and $\tau_2 = 2$. We compute the numerical solutions by both the ADP and SDP methods and present the numerical results in Figure 4.6. As one can see, the obtained results are now very different. In order to verify whether the proposed ADP method captures the detonation wave propagating with the correct speed, we compute the reference solution computed using the unsplit central-upwind scheme for the fast, but finite reaction time with $1/\varepsilon_1 = 1/\varepsilon_2 = 10^6$. The reference solution is computed using $\Delta x = 1/1000$, and as it agrees well with the ADP solution, we conclude that the ADP solution is capable of accurately capturing the correct detonation wave speed, while the SDP method fails.

Example 9b–1-D stiff case. Next, we study the 1-D stiff case using an example similar to the one considered in [37]. We take the following Riemann initial data:

$$(\rho,u,p,z_1,z_2,z_3,z_4,z_5)(x,0) = \begin{cases} (2,10,40,0,0,0.17,0.63,0.2), & \text{if } x \le 0.5, \\ (1,0,1,0.08,0.72,0,0,0.2), & \text{if } x > 0.5, \end{cases}$$

and set $q_3 = -100$. We first compute the solution with $\tau_1 = \tau_2 = 1.5$ and $1/\varepsilon_1 = 1/\varepsilon_2 = 10^5$ (which were used in [37]) until the final time $t = 0.06$ by both the ADP and SDP methods

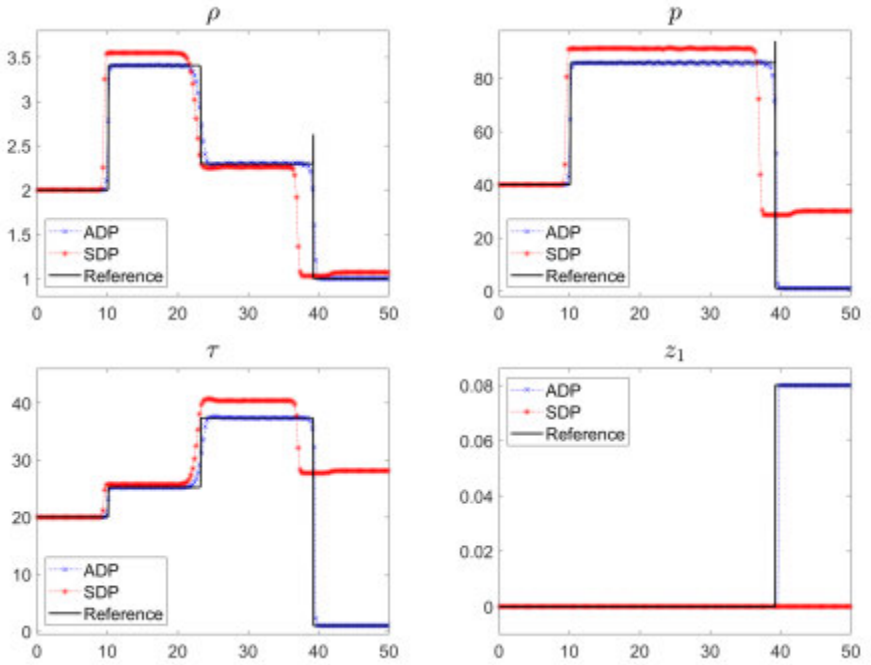

FIG. 4.6. *Example 9a: Same as in Figure 4.5, but for* $\tau_1 = 1.5$ *and* $\tau_2 = 2$.

on the domain $[0,2]$ using a uniform mesh with $\Delta x = 1/150$. The obtained results (pressure, temperature, mass fractions of H_2 and OH) are plotted in Figure 4.7 together with the reference solution computed by the unsplit central-upwind scheme with a much finer uniform spatial mesh with $\Delta x = 1/5000$. It should be observed that the reference solution can be, in principle, computed on a coarser grid, but the use of any mesh size $\Delta x \gtrsim 1/400$ will lead to inaccurate solution. This suggests that this case is stiff but not very stiff. As can be clearly seen, the SDP methods fails to capture the correct speed of the detonation wave, while the ADP method shows a good agreement with the reference solution; see also the numerical solution reported in [37, Example 5.3]. At the same time, one can observe that the mass fractions of H_2 and OH have small jumps at $x = 0.5$, which is the breaking point in the initial data, and also their values are quite inaccurate in the post detonation wave area, which is at $x \in [0.8, 1.3]$. We believe that this is attributed to the fact that the ignition temperatures are quite low in this example. While the above results may be considered satisfactory (recall that the aim of this paper is to develop an underresolved method capable of exactly capturing the speed of the detonation wave), the gain in the efficiency is rather small as this particular set of data corresponds to a not very stiff case. We therefore investigate the behavior of the ADP method for the same set of the ignition temperatures, that is, $\tau_1 = \tau_2 = 1.5$, but 10 times larger $1/\varepsilon_1 = 1/\varepsilon_2 = 10^6$. We then compute the ADP solution at the same final time $t = 0.06$ using the same coarse grid as before ($\Delta x = 1/150$) and plot it in Figure 4.8 along with the reference solution computed with $\Delta x = 1/10000$. As one can see, the ADP method fails. We then refine the mesh to $\Delta x = 1/600$ and observe that in this case, the ADP method produces accurate results, which are close to the reference solution; see Figure 4.8. However, the unsplit central-upwind scheme, used to

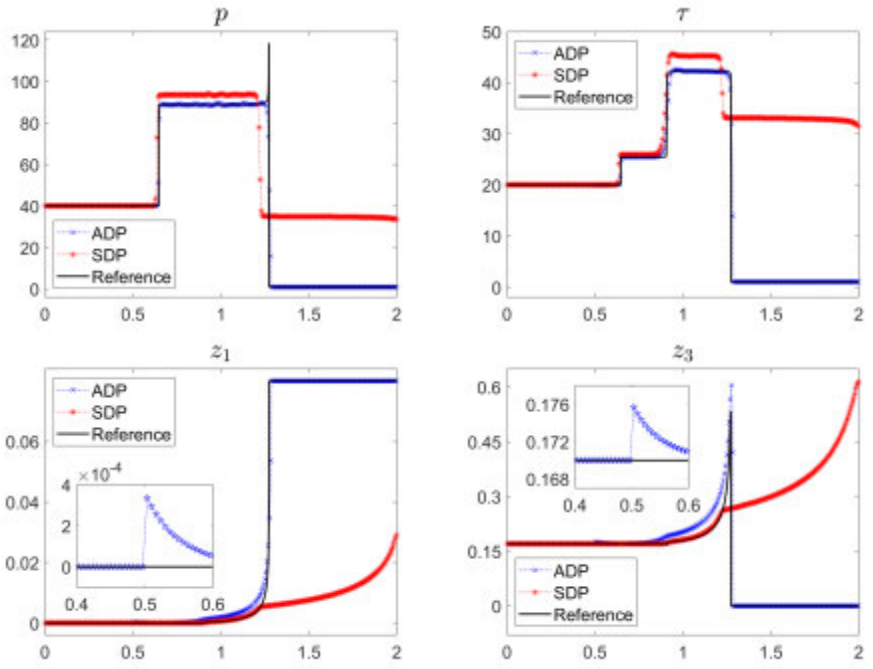

FIG. 4.7. *Example 9b: Pressure (p), temperature (τ), mass fraction of* H_2 *(z_1) and mass fraction of* OH *(z_3) computed by the ADP and SDP methods for $\tau_1=\tau_2=1.5$ and $1/\varepsilon_1=1/\varepsilon_2=10^5$. The small jumps in z_1 and z_3 occurring at $x=0.5$ are magnified.*

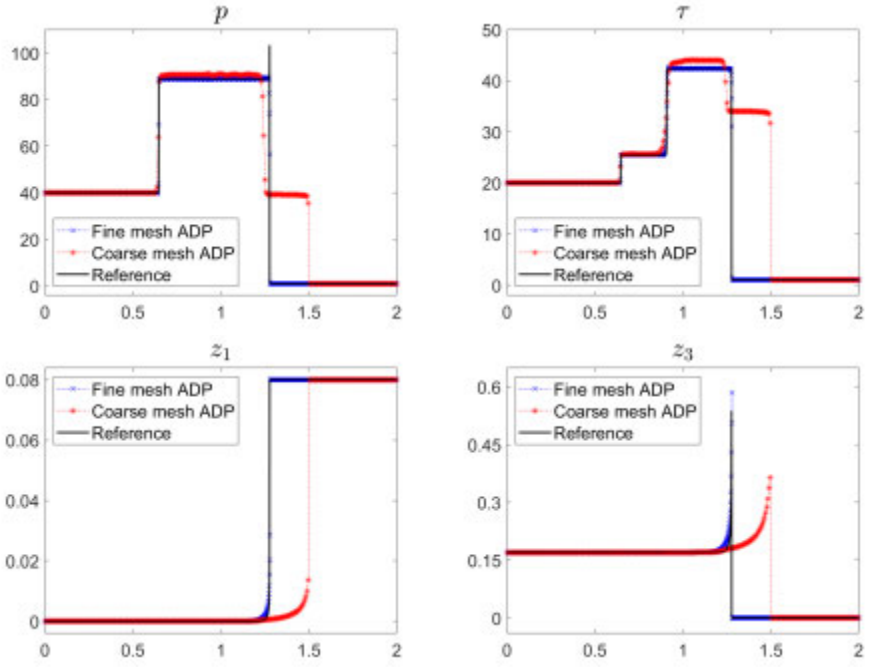

FIG. 4.8. *Example 9b: Pressure (p), temperature (τ), mass fraction of* H_2 *(z_1) and mass fraction of* OH *(z_3) computed by the ADP method with $\Delta x=1/150$ and $1/600$ for $1/\varepsilon_1=1/\varepsilon_2=10^6$.*

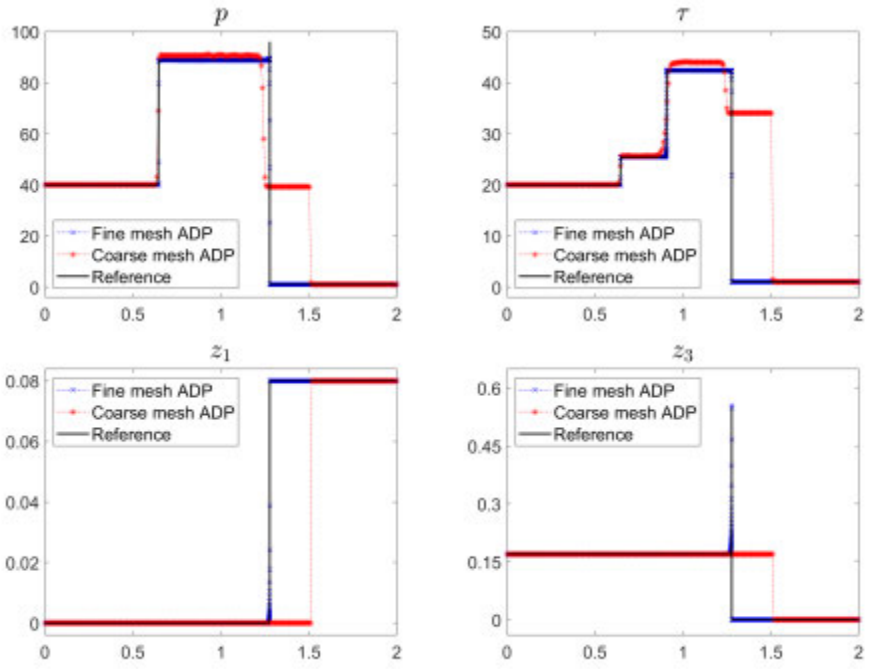

FIG. 4.9. *Example 9b: Same as in Figure 4.8, but for* $1/\varepsilon_1 = 1/\varepsilon_2 = 10^7$.

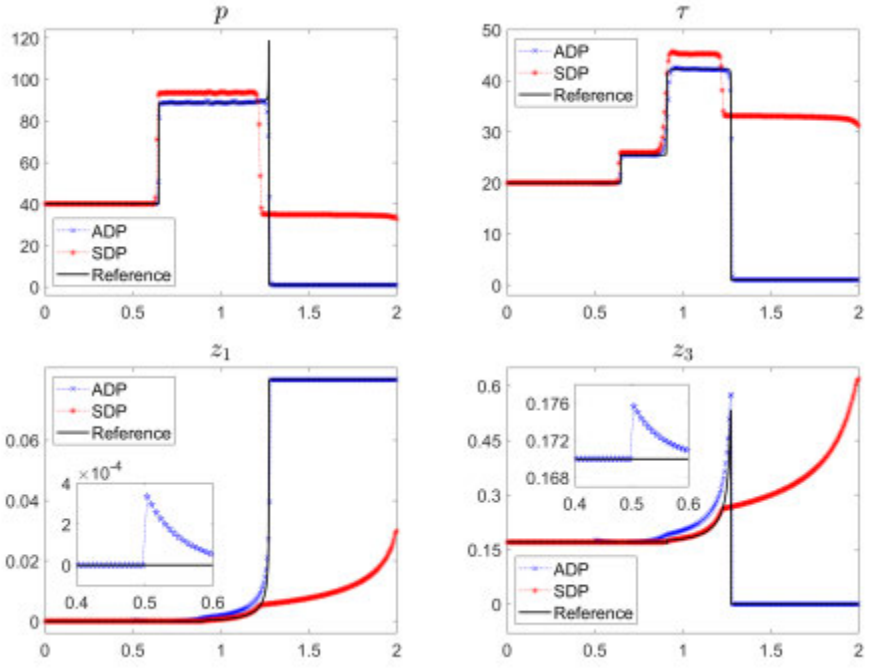

FIG. 4.10. *Example 9b: Same as in Figure 4.7, but with* $\tau_1 = \tau_2 = 2$.

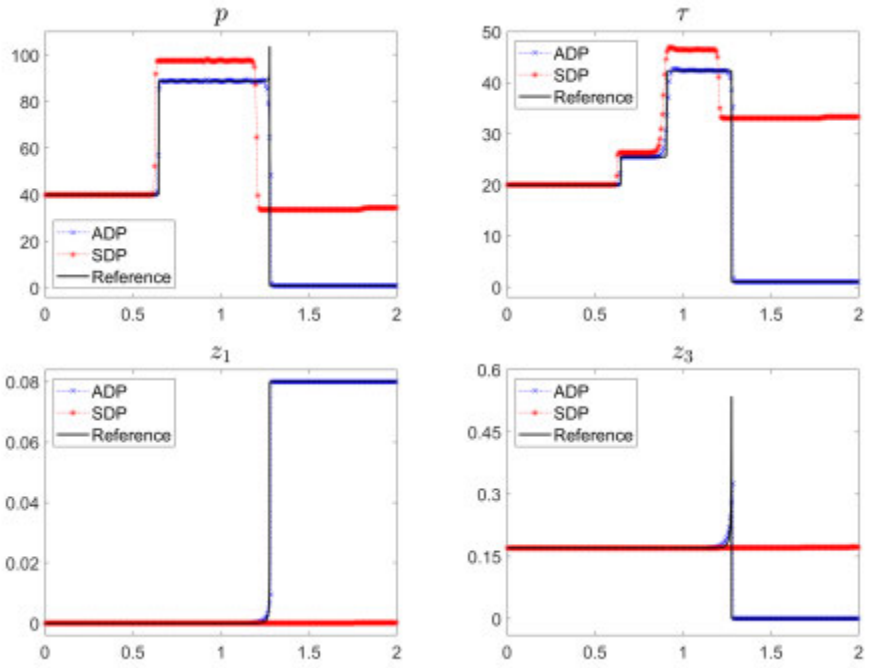

FIG. 4.11. *Example 9b: Same as in Figure 4.10, but with* $1/\varepsilon_1 = 1/\varepsilon_2 = 10^6$.

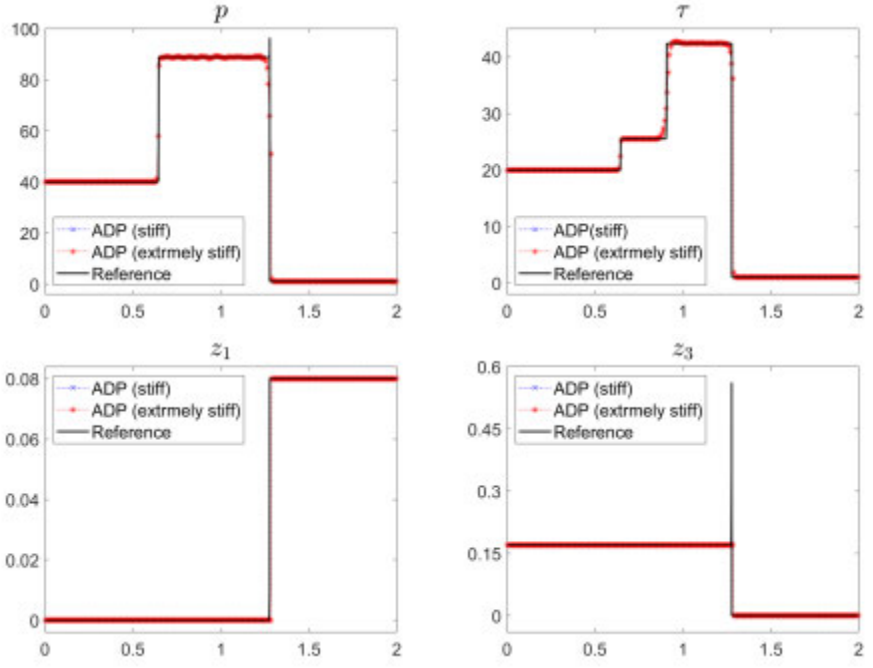

FIG. 4.12. *Example 9b: Pressure* (p)*, temperature* (τ)*, mass fraction of* H_2 (z_1) *and mass fraction of* OH (z_3) *computed by the stiff and extremely stiff ADP methods for* $1/\varepsilon_1 = 1/\varepsilon_2 = 10^7$.

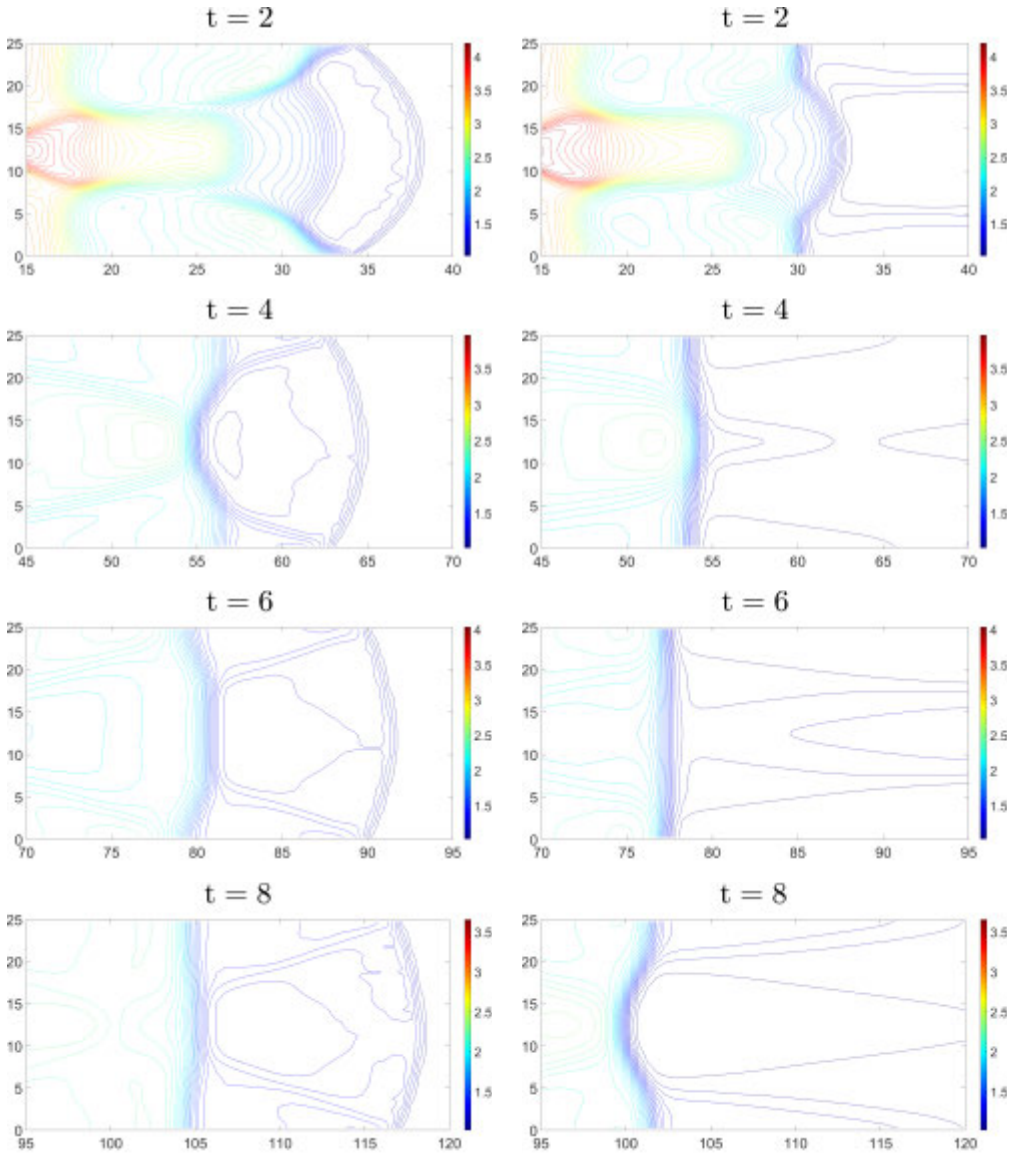

FIG. 4.13. *Example 9c: Contour plots of density (ρ) computed by the ADP (left column) and SDP (right column) methods at different times.*

produce the reference solution, is capable of accurately capturing the detonation wave speed using a mesh with $\Delta x \lesssim 1/3200$, which means that the efficiency gain achieved by the ADP method is more substantial than in the previously considered less stiff regime.

We then reduce the reaction time even further and take $1/\varepsilon_1 = 1/\varepsilon_2 = 10^7$. We compute the ADP and reference solutions until the same final time $t = 0.06$ and plot the obtained results in Figure 4.9. As one can see, when the ADP method is used on a coarse mesh with $\Delta x = 1/150$, the computed detonation wave propagates with a wrong speed. In order to achieve the correct speed, one has to take a much finer mesh: after reducing the reaction times by a factor of 10, we had to take $\Delta x = 1/6000$, which is also

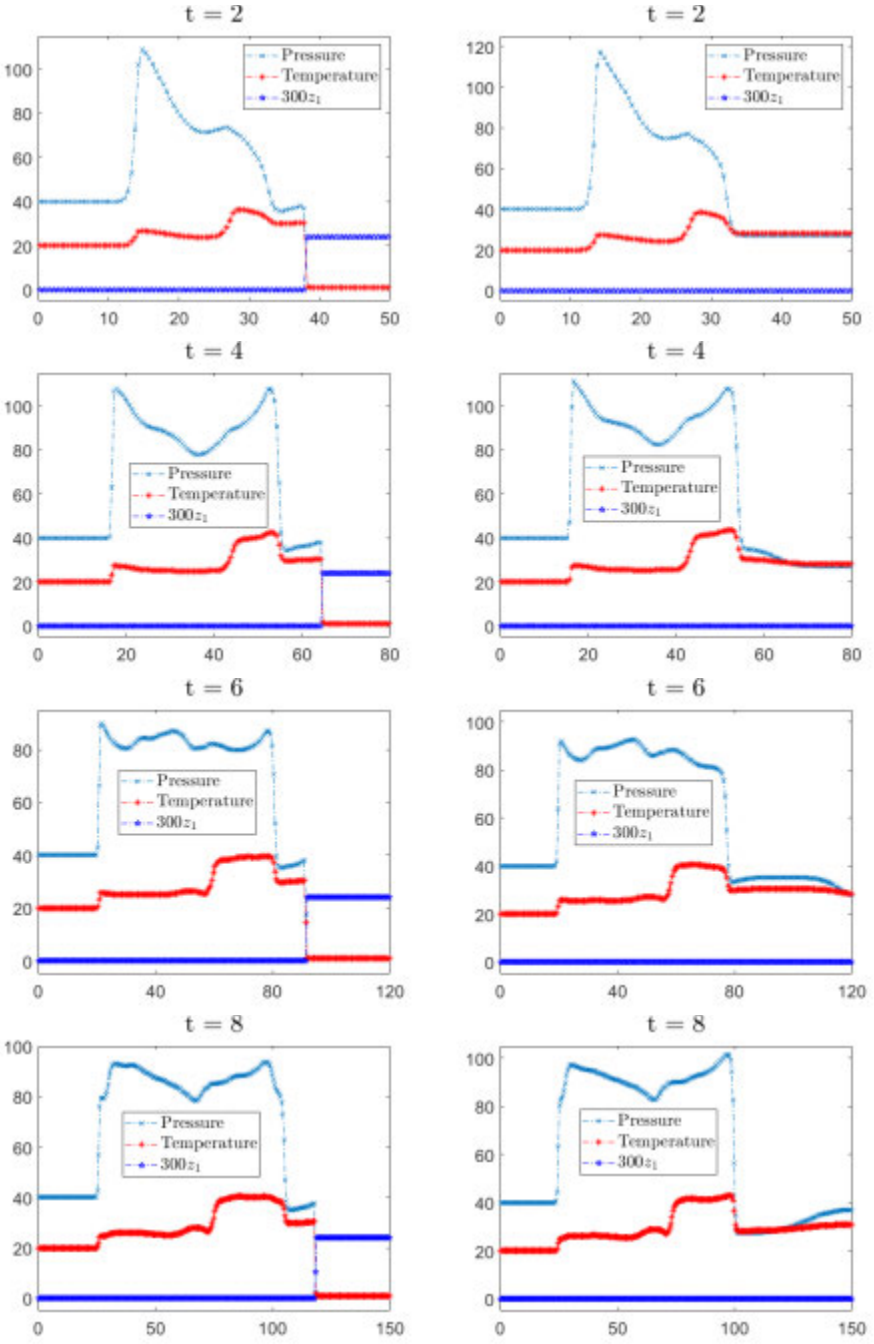

FIG. 4.14. *Example 9c: Pressure (p), temperature (τ) and 300 times mass fraction of* H_2 *($300z_1$) computed by the ADP (left column) and SDP (right column) methods at different times.*

10 times smaller and this is about the borderline. This implies that the mesh size should be proportional to the reaction time and thus the ADP method cannot be used as an underresolved method. Nevertheless, it is instructive to compare the ADP solutions with the reference solution, which is computed with $\Delta x = 1/50000$ in Figure 4.9. In

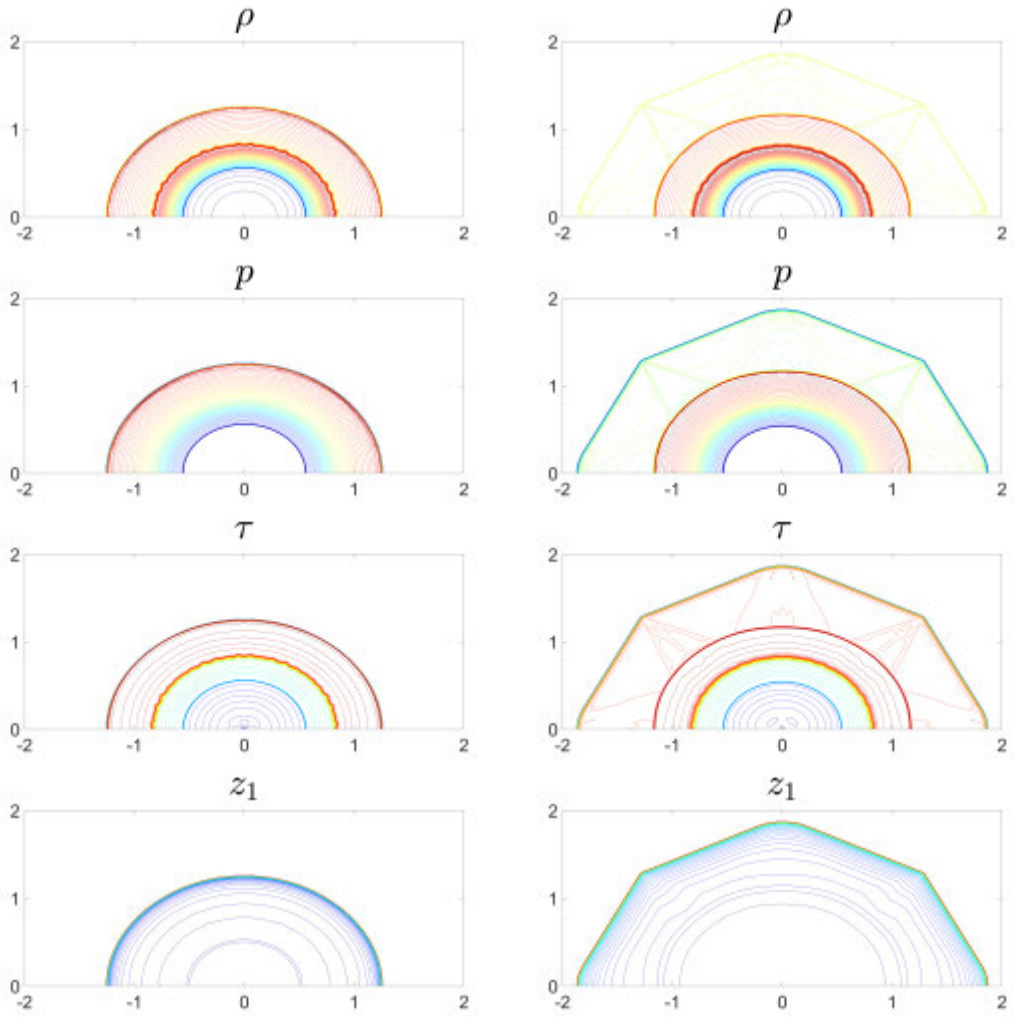

FIG. 4.15. *Example 9d: Density (ρ), pressure (p), temperature (τ) and mass fraction of* H_2 *(z_1) computed by the ADP (left column) and SDP (right column) methods with* $\Delta x = \Delta y = 1/200$.

fact, the unsplit central-upwind scheme can capture the detonation wave propagating with the accurate speed with a slightly larger Δx as long as $\Delta x \lesssim 1/32000$, which means that the ADP method is still more efficient. However, it clearly becomes impractical in a very stiff regime with small ignition temperatures.

Based on the above observations, we conjecture that the low efficiency of the ADP method in the considered numerical example is related to the fact that the ignition temperatures are low. We therefore proceed with the investigation of the solution behavior when the ignition temperatures are slightly larger. To this end, we take $\tau_1 = \tau_2 = 2$ and consider several different sets of the reaction times. We begin with $1/\varepsilon_1 = 1/\varepsilon_2 = 10^5$ and compute the numerical solutions by both the ADP and SDP methods until the same final time $t = 0.06$. In Figure 4.10, we present the results obtained with $\Delta x = 1/150$ together with the reference solution computed by the unsplit central-upwind scheme using $\Delta x = 1/5000$. As one can see, the ADP solution is reasonably accurate though,

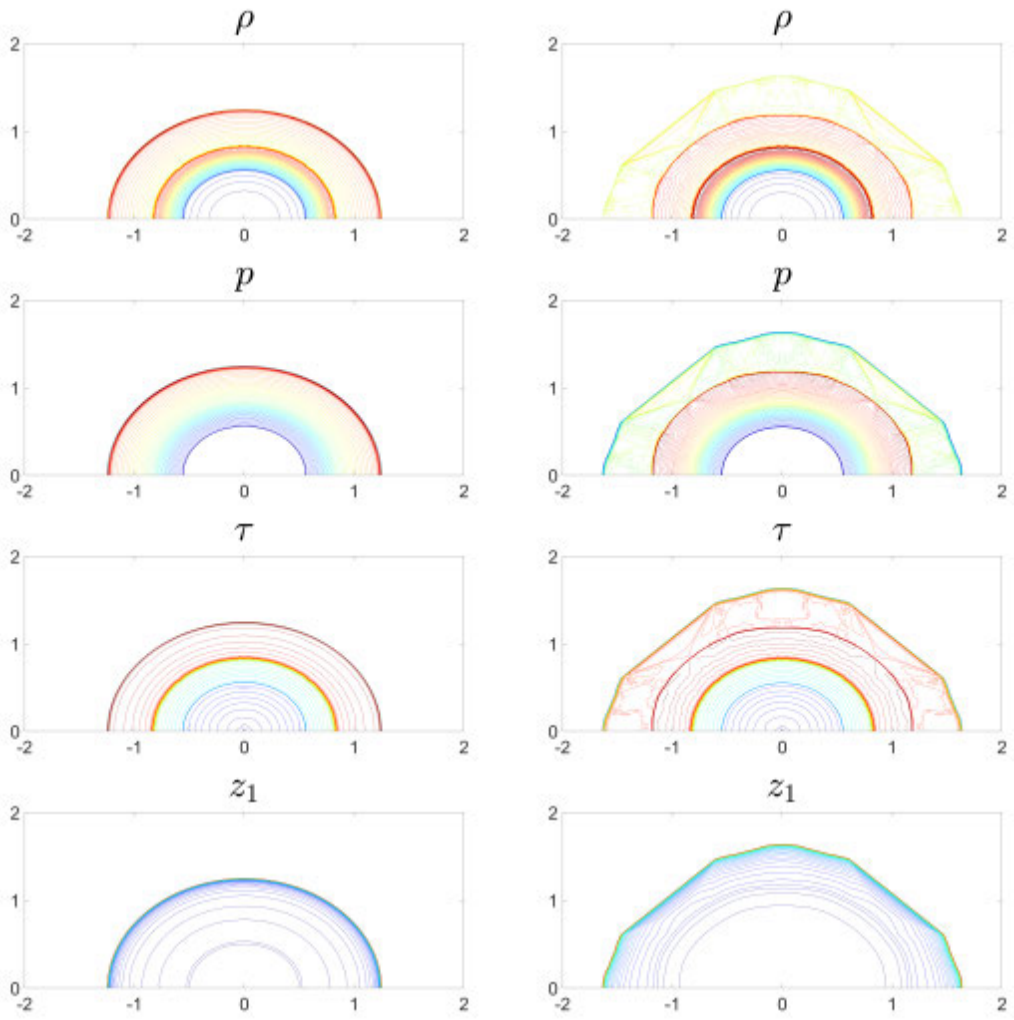

FIG. 4.16. *Example 9d: Same as in Figure 4.15, but for* $\Delta x = \Delta y = 1/400$.

as in the case of the lower ignition temperature (see Figure 4.7), it still has a small jump in the mass fractions at $x = 0.5$ and the computed mass fraction values are quite inaccurate in the post detonation wave area, which is at $x \in [0.8, 1.3]$. At the same time, the SDP method clearly fails. We emphasize that the case of $1/\varepsilon_1 = 1/\varepsilon_2 = 10^5$ is, as before, not very stiff since the unsplit central-upwind scheme could have captured the accurate propagation of the detonation wave as long as $\Delta x \lesssim 1/250$.

We then reduce the reaction times and take $1/\varepsilon_1 = 1/\varepsilon_2 = 10^6$ without changing any other data. In Figure 4.11, we plot the ADP and SDP solutions computed on a coarse mesh with $\Delta x = 1/150$ along with the reference solution computed with $\Delta x = 1/10000$. As one can see, the SDP solution is wrong, while the ADP solution is quite accurate. We also note that the efficiency gain is more substantial now as the unsplit central-upwind scheme can be used with $\Delta x \lesssim 1/2500$ only.

We finish this set of experiments by considering even smaller reaction times with $1/\varepsilon_1 = 1/\varepsilon_2 = 10^7$ and computing the numerical solutions by the ADP method on a coarse

mesh with $\Delta x=1/150$. The obtained results are depicted in Figure 4.12 together with the reference solution computed using $\Delta x=1/50000$ and the ADP solution computed in the extremely stiff setting. As one can see, the obtained solutions are in very good agreement, which confirms that the ADP method is applicable and very efficient in the case of larger ignition temperatures. We also mention that the efficiency gain is now even more crucial as the unsplit central-upwind scheme requires the mesh size to be $\Delta x\lesssim 1/30000$.

Example 9c–2-D extremely stiff case. We now consider the 2-D extremely stiff case with the initial data taken from [4, Example 5.6]:

$$(\rho,u,v,p,z_1,z_2,z_3,z_4,z_5)(x,y,0)=\begin{cases}(2,10,0,40,0,0,0.17,0.63,0.2), & \text{if } r\le\xi(y),\\ (1,0,0,1,0.08,0.72,0,0,0.2), & \text{if } r>\xi(y),\end{cases}$$

where $r=\sqrt{x^2+y^2}$ and

$$\xi(y)=\begin{cases}12.5-|y-12.5|, & \text{if } |y-12.5|\le 7.5,\\ 5, & \text{if } |y-12.5|>7.5.\end{cases}$$

In this example, we set $q_3=-40$, $\tau_1=2$, $\tau_2=10$, and use the ADP operator (4.11) with the same projection mass fraction values, which were used in Example 9a, namely, $z_1^{HT}=0$, $z_1^{IT}=0.035$, $z_1^{LT}=0.08$, $z_2^{HT}=0$, $z_2^{IT}=0$, $z_2^{LT}=0.72$, $z_3^{HT}=0.17$, $z_3^{IT}=0.765$ and $z_3^{LT}=0$. The problem is solved in the computational domain $[0,150]\times[0,25]$ using a uniform mesh with $\Delta x=\Delta y=1/2$. Solid wall boundary conditions are implemented along the boundaries $y=0$ and $y=25$, and free boundary conditions are used at $x=0$ and $x=150$. In Figure 4.13, we show contour plots of the density computed by both the ADP and SDP methods at times $t=2$, 4, 6 and 8. We also plot, in Figure 4.14, profiles of pressure, temperature and 300 times mass fraction of H_2 (as before, we plot $300z_1$ rather then z_1 for a better visualization) along the line $y=12.5$ at the same times. As one can clearly see from these figures, the ADP and SDP solutions are very different in this example. As the ADP solution agrees well with the one reported in [4, Example 5.6], we conclude that the ADP method captures the detonation wave propagating with the correct speeds.

Example 9d–2-D stiff case. In the last example, we consider the 2-D case with the radially symmetric initial data given by

$$(\rho,u,v,p,z_1,z_2,z_3,z_4,z_5)(x,y,0)=\begin{cases}(2,u_{\text{in}}(x,y),v_{\text{in}}(x,y),40,0,0,0.17,0.63,0.2), & r\le 0.5,\\ (1,0,0,1,0.08,0.72,0,0,0.2), & r>0.5,\end{cases}$$

where $r=\sqrt{x^2+y^2}$, $u_{\text{in}}(x,y)=10x/r$ and $v_{\text{in}}(x,y)=10y/r$. Other parameters are the same as in Example 9c: $q_3=-100$, $\tau_1=\tau_2=1.5$ and $1/\varepsilon_1=1/\varepsilon_2=10^5$. We compute the solution until the final time $t=0.06$ by both the ADP and SDP methods in the computational domain $[-2,2]\times[0,2]$ using a uniform mesh with $\Delta x=\Delta y=1/200$. The solid wall boundary conditions are used along the bottom part of the domain, while the free boundary conditions are implemented at the other parts of the boundary. Contour plots of the density, pressure, temperature and mass fraction of H_2 are presented in Figure 4.15. As one can clearly see, the results obtained by the ADP and SDP methods are very different. In order to verify that the ADP solution converges to the physically relevant one, we compute the solutions by both the ADP and SDP methods using a finer mesh with $\Delta x=\Delta y=1/400$ and present the results in Figure 4.16. As one can see, the position of the detonation wave in the obtained ADP solutions is about the same,

which suggests that the ADP method captures the detonation wave propagating with the correct speed. On contrary, the SDP solution is clearly mesh dependent and thus it fails.

5. Comparison with existing methods

It is instructive to compare the proposed ADP method with an existing high-order method. To this end, we have repeated the same computations as in Example 8b with $1/\varepsilon_1 = 2 \times 10^5$ using the high-order subcell resolution method from [32]. This is a fractional step method. In the convection step, a fifth-order finite-difference WENO scheme has been implemented using the local Lax-Friedrichs flux splitting and the local characteristic decomposition together with the three-stage third-order SSP Runge-Kutta method from [10,11]. In the reaction step, the same ODE solver has been used but with certain computed flow variables in the shock region modified by the Harten subcell resolution idea.

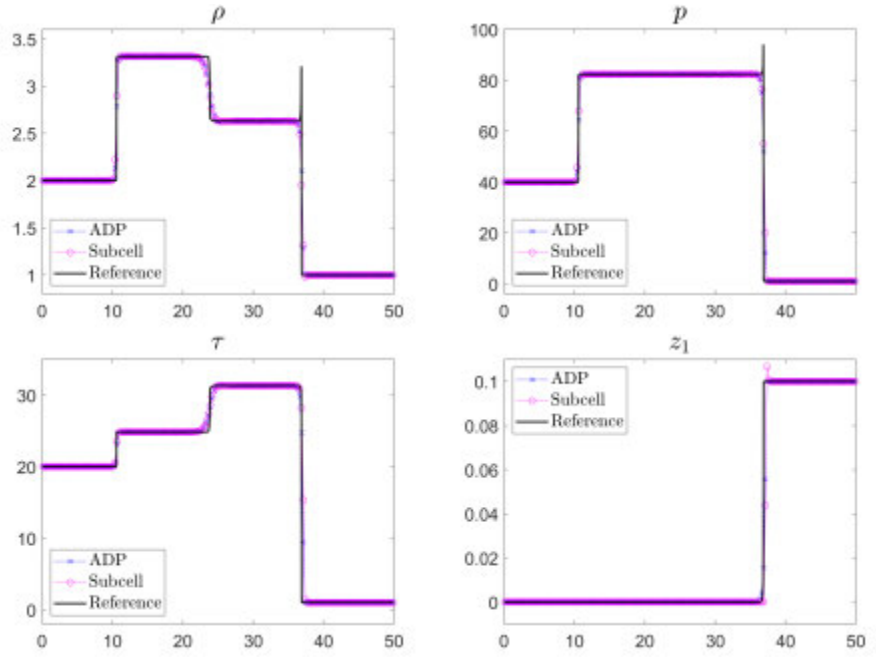

FIG. 5.1. *Example 8b (additional comparison): Density (ρ), pressure (p), temperature (τ) and mass fraction of CH_4 (z_1) computed by the ADP and high-order subcell resolution methods for* $1/\varepsilon_1 = 2 \times 10^5$.

In Figure 5.1, the results obtained by the subcell resolution method are compared with the corresponding ADP solution and the reference solution, which have been previously shown in Figure 4.2. As one can clearly see, the results obtained by the ADP and subcell resolution methods are very close, which, once again, suggests that the ADP method is quite accurate and capable of exactly capturing the propagation of detonation waves.

It is worth noting that as mentioned in [32], the high-order subcell resolution method required a relatively small CFL number. In addition, it required the reaction splitting substep (at which the ODEs for the mass fractions to be numerically integrated) to consist of many small time steps to obtain a stable solution and the number of these time steps increases proportionally to the stiffness of the problem at hand, which affects

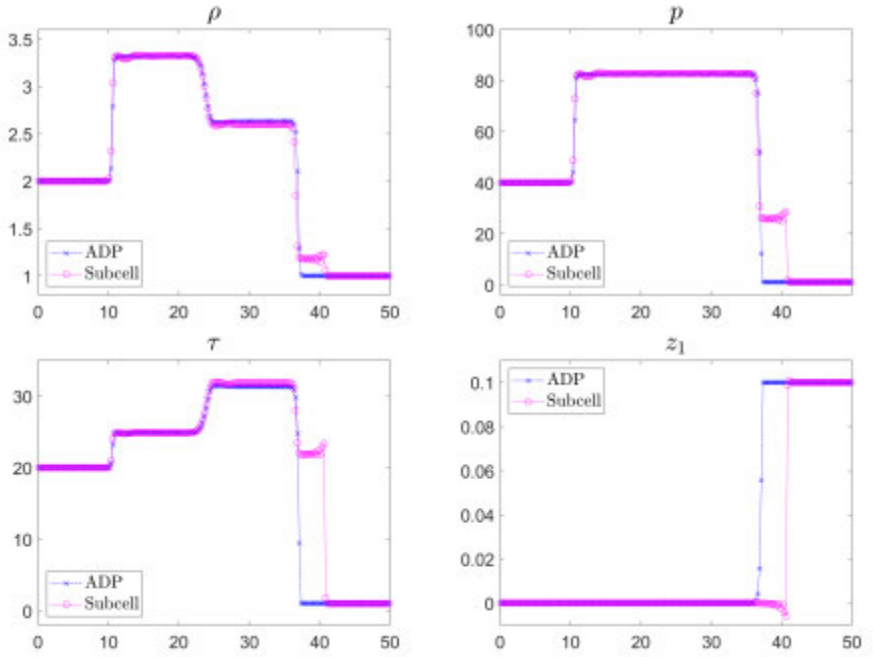

FIG. 5.2. *Example 8b (additional comparison): Density (ρ), pressure (p), temperature (τ) and mass fraction of* CH_4 *(z_1) computed by the ADP and high-order subcell resolution method with the CFL number 0.3 and only 1 reaction ODE time step for* $1/\varepsilon_1 = 2\times 10^5$.

the efficiency of the subcell resolution method. For instance, in order to obtain the subcell resolution results shown in Figure 5.1, we have taken the CFL number 0.1 and 100 reaction ODE time steps as in [32, Example 5.2]. However, if a larger CFL number and a smaller number of reaction time steps are used in the computations, the subcell resolution method from [32] may produce detonation waves propagating with a wrong speed. In order to illustrate this, we take the CFL number 0.3 and 1 reaction ODE time step (as in the ADP method), recompute the results by the high-order subcell resolution method, and depict them in Figure 5.2. As one can see, the detonation wave now propagates with a wrong speed, which is not the case when the proposed second-order ADP method is implemented. In the future work, we plan to extend the ADP method to the fifth order of accuracy via the alternative weighted essentially non-oscillatory (A-WENO) framework.

6. Conclusion

In this paper, we have considered inviscid, compressible, reactive flows governed by the Euler equations coupled with a transport equation for the fraction of unburnt gas. For small reaction times, the chemical reaction may be considered infinitely fast and thus the transport equation has a stiff source term, which can be efficiently treated by projecting the computed solution onto an equilibrium state. A straightforward projection however has a major drawback: it may lead to a spurious detonation wave that travels with a nonphysical speed even if the scheme is stable, as we illustrated in our numerical examples. Here, we have shown how the "standard" deterministic projection approach can be modified to provide an accurate approximation for the underlying model. As the result, we have designed a simple, robust and stable underresolved method for stiff detonation waves using an accurate deterministic projection (ADP) approach and

demonstrated that the proposed computational technique guarantees that the detonation waves will propagate with a physically relevant speed. For the stiff waves, when the chemical reaction time scales are not so much faster than the fluid dynamical ones, the chemical reaction may not be considered infinitely fast. Otherwise, many details in the reaction will be hidden. For this reason, we extend the proposed ADP method for solving the stiff cases. We also extend the ADP method to 1-D and 2-D multispecies waves, including extremely stiff and stiff cases. A number of numerical examples have been presented to show the good performance of the proposed ADP method.

Acknowledgment. The work of A. Chertock was supported in part by NSF grants DMS-1818684 and DMS-2208438. The work of A. Kurganov was supported in part by NSFC grants 12171226 and 12111530004, and by the fund of the Guangdong Provincial Key Laboratory of Computational Science and Material Design (No. 2019B030301001). We would like to acknowledge the contribution of Yunlong Chen and Minlan Lei, who worked on the development of the two-dimensional accurate deterministic projection method for the extremely stiff regime as a part of their M.Sc. studies at Tulane University in 2011–2012. We would like to thank the authors of [32], who kindly provided us with their code, which was used to generate the numerical results in [32] and in Figures 5.1 and 5.2.

Appendix. Semi-discrete central-upwind scheme. In this section, we briefly describe the semi-discrete central-upwind scheme for the homogeneous 2-D systems (2.1), (1.3) and (2.4), (1.3). The 2-D semi-discrete central-upwind scheme from [21] admits the following flux form:

$$\frac{\mathrm{d}}{\mathrm{d}t}\overline{\boldsymbol{U}}_{j,k}(t)=-\frac{\boldsymbol{H}^x_{j+\frac12,k}-\boldsymbol{H}^x_{j-\frac12,k}}{\Delta x}-\frac{\boldsymbol{H}^y_{j,k+\frac12}-\boldsymbol{H}^y_{j,k-\frac12}}{\Delta y}, \tag{A.1}$$

where the numerical fluxes are

$$\begin{aligned}
\boldsymbol{H}^x_{j+\frac12,k}&=\frac{a^+_{j+\frac12,k}\boldsymbol{F}(\boldsymbol{U}^{\mathrm{E}}_{j,k})-a^-_{j+\frac12,k}\boldsymbol{F}(\boldsymbol{U}^{\mathrm{W}}_{j+1,k})}{a^+_{j+\frac12,k}-a^-_{j+\frac12,k}}+\frac{a^+_{j+\frac12,k}a^-_{j+\frac12,k}}{a^+_{j+\frac12,k}-a^-_{j+\frac12,k}}\left[\boldsymbol{U}^{\mathrm{W}}_{j+1,k}-\boldsymbol{U}^{\mathrm{E}}_{j,k}\right],\\
\boldsymbol{H}^y_{j,k+\frac12}&=\frac{b^+_{j,k+\frac12}\boldsymbol{G}(\boldsymbol{U}^{\mathrm{N}}_{j,k})-b^-_{j,k+\frac12}\boldsymbol{G}(\boldsymbol{U}^{\mathrm{S}}_{j,k+1})}{b^+_{j,k+\frac12}-b^-_{j,k+\frac12}}+\frac{b^+_{j,k+\frac12}b^-_{j,k+\frac12}}{b^+_{j,k+\frac12}-b^-_{j,k+\frac12}}\left[\boldsymbol{U}^{\mathrm{N}}_{j,k+1}-\boldsymbol{U}^{\mathrm{S}}_{j,k}\right].
\end{aligned} \tag{A.2}$$

The quantities $\overline{\boldsymbol{U}}_{j,k}$, $\boldsymbol{H}^x_{j,k}$, $\boldsymbol{H}^y_{j,k}$, $a^+_{j,k}$, $a^-_{j,k}$, $\boldsymbol{U}^{\mathrm{E}}_{j,k}$, $\boldsymbol{U}^{\mathrm{W}}_{j,k}$, $\boldsymbol{U}^{\mathrm{N}}_{j,k}$ and $\boldsymbol{U}^{\mathrm{S}}_{j,k}$ depend in fact on t, but we suppress this dependence for the sake of brevity.

In (A.2),

$$\begin{aligned}
&\boldsymbol{U}^{\mathrm{E}}_{j,k}=\overline{\boldsymbol{U}}_{j,k}+\frac{\Delta x}{2}(\boldsymbol{U}_x)_{j+\frac12,k},\boldsymbol{U}^{\mathrm{W}}_{j,k}=\overline{\boldsymbol{U}}_{j,k}-\frac{\Delta x}{2}(\boldsymbol{U}_x)_{j+\frac12,k},\\
&\boldsymbol{U}^{\mathrm{N}}_{j,k}=\overline{\boldsymbol{U}}_{j,k}+\frac{\Delta y}{2}(\boldsymbol{U}_y)_{j,k+\frac12},\ \ \boldsymbol{U}^{\mathrm{S}}_{j,k}=\overline{\boldsymbol{U}}_{j,k}-\frac{\Delta y}{2}(\boldsymbol{U}_y)_{j,k+\frac12}
\end{aligned}$$

are the point values of the piecewise linear reconstruction

$$\widetilde{\boldsymbol{U}}(x,y)=\overline{\boldsymbol{U}}_{j,k}+(\boldsymbol{U}_x)_{j,k}(x-x_j)+(\boldsymbol{U}_y)_{j,k}(y-y_k),\quad (x,y)\in\left(x_{j-\frac12},x_{j+\frac12}\right)\times\left(y_{k-\frac12},y_{k+\frac12}\right)$$

at the midpoints of the edges of cell (j,k).

The numerical derivatives $(\boldsymbol{U}_x)_{j,k}$ and $(\boldsymbol{U}_y)_{j,k}$ are to be computed using a nonlinear limiter. We have used a minmod limiter (see, e.g., [24, 27, 30]), which gives

$$(\boldsymbol{U}_x)_{j,k}=\mathrm{minmod}\left(\frac{\overline{\boldsymbol{U}}_{j+1,k}-\overline{\boldsymbol{U}}_{j,k}}{\Delta x},\theta\frac{\overline{\boldsymbol{U}}_{j+1,k}-\overline{\boldsymbol{U}}_{j-1,k}}{2\Delta x},\frac{\overline{\boldsymbol{U}}_{j,k}-\overline{\boldsymbol{U}}_{j-1,k}}{\Delta x}\right),$$

$$(\boldsymbol{U}_y)_{j,k}=\text{minmod}\left(\frac{\overline{\boldsymbol{U}}_{j,k+1}-\overline{\boldsymbol{U}}_{j,k}}{\Delta y},\theta\frac{\overline{\boldsymbol{U}}_{j,k+1}-\overline{\boldsymbol{U}}_{j,k-1}}{2\Delta y},\frac{\overline{\boldsymbol{U}}_{j,k}-\overline{\boldsymbol{U}}_{j,k-1}}{\Delta y}\right),$$

where $\theta\in[1,2]$ can be used to control the amount of numerical dissipation present in the resulting scheme and larger θ's correspond to less dissipative but, in general, more oscillatory reconstructions. The minmod function is defined as

$$\text{minmod}(a,b):=\frac{\text{sgn}(a)+\text{sgn}(b)}{2}\cdot\min(|a|,|b|).$$

One-sided local propagation speeds in the x- and y-directions $a^{\pm}_{j+\frac12,k}$ and $b^{\pm}_{j,k+\frac12}$ are obtained using the largest/smallest eigenvalues of the Jacobian. For the reactive Euler systems (2.1), (1.3) and (2.4), (1.3), we obtain

$$a^{+}_{j+\frac12,k}=\max\left(u^{\rm E}_{j,k}+\sqrt{\frac{\gamma p^{\rm E}_{j,k}}{\rho^{\rm E}_{j,k}}},u^{\rm W}_{j+1,k}+\sqrt{\frac{\gamma p^{\rm W}_{j+1,k}}{\rho^{\rm W}_{j,k}}},0\right),$$

$$a^{-}_{j+\frac12,k}=\min\left(u^{\rm E}_{j,k}-\sqrt{\frac{\gamma p^{\rm E}_{j,k}}{\rho^{\rm E}_{j,k}}},u^{\rm W}_{j+1,k}-\sqrt{\frac{\gamma p^{\rm W}_{j+1,k}}{\rho^{\rm W}_{j,k}}},0\right),$$

$$b^{+}_{j,k+\frac12}=\max\left(u^{\rm N}_{j,k}+\sqrt{\frac{\gamma p^{\rm N}_{j,k}}{\rho^{\rm N}_{j,k}}},u^{\rm S}_{j,k+1}+\sqrt{\frac{\gamma p^{\rm S}_{j,k+1}}{\rho^{\rm S}_{j,k}}},0\right),$$

$$b^{-}_{j,k+\frac12}=\min\left(u^{\rm N}_{j,k}-\sqrt{\frac{\gamma p^{\rm N}_{j,k}}{\rho^{\rm N}_{j,k}}},u^{\rm S}_{j,k+1}-\sqrt{\frac{\gamma p^{\rm S}_{j,k+1}}{\rho^{\rm S}_{j,k}}},0\right).$$

Finally, the ODE system (A.1) is numerically integrated by the three-stage third-order strong stability preserving (SSP) Runge-Kutta method; see, [10, 11].

REFERENCES

[1] M. Arienti and J.E. Shepherd, *A numerical study of detonation diffraction*, J. Fluid Mech., 529:117–146, 2005. 3.1

[2] W. Bao and S. Jin, *The random projection method for hyperbolic conservation laws with stiff reaction terms*, J. Comput. Phys., 163:216–248, 2000. 1, 2.3

[3] W. Bao and S. Jin, *The random projection method for stiff detonation capturing*, SIAM J. Sci. Comput., 23:1000–1026, 2001. 1, 2.3, 2.3

[4] W. Bao and S. Jin, *The random projection method for stiff multispecies detonation capturing*, J. Comput. Phys., 178:37–57, 2002. 1, 4, 4.3, 4.3, 4.3, 4.3, 4.3, 4.3, 4.3, 4.3

[5] A.C. Berkenbosch, E.F. Kaasschieter, and R. Klein, *Detonation capturing for stiff combustion chemistry*, Combust. Theory Model., 2:313–348, 1998. 1

[6] A. Bourlioux, A.J. Majda, and V. Roytburd, *Theoretical and numerical structure for unstable one-dimensional detonations*, SIAM J. Appl. Math., 51:303–343, 1991. 1

[7] A. Chertock and A. Kurganov, *On a practical implementation of particle methods*, Appl. Numer. Math., 56:1418–1431, 2006. 1

[8] P. Colella, A. Majda, and V. Roytburd, *Fractional step methods for reacting shock waves*, in G. Ludford (ed.), Reacting Flows: Combustion and Chemical Reactors, Part 2 (Ithaca, N.Y., 1985), Lectures in Appl. Math., Amer. Math. Soc., Providence, RI, 24, 1986. 1

[9] P. Colella, A. Majda, and V. Roytburd, *Theoretical and numerical structure for reacting shock waves*, SIAM J. Sci. Statist. Comput., 7:1059–1080, 1986. 1

[10] S. Gottlieb, D. Ketcheson, and C.W. Shu, *Strong Stability Preserving Runge-Kutta and Multistep Time Discretizations*, World Scientific Publishing Co. Pte. Ltd., Hackensack, NJ, 2011. 5, 6

[11] S. Gottlieb, C.W. Shu, and E. Tadmor, *Strong stability-preserving high-order time discretization methods*, SIAM Rev., 43:89–112, 2001. 5, 6

[12] C. Helzel, R.J. Leveque, and G. Warnecke, *A modified fractional step method for the accurate approximation of detonation waves*, SIAM J. Sci. Comput., 22:1489–1510, 2000. 1
[13] W.D. Henshaw and D.W. Schwendeman, *An adaptive numerical scheme for high-speed reactive flow on overlapping grids*, J. Comput. Phys., 191:420–447, 2003. 1
[14] W.D. Henshaw and D.W. Schwendeman, *Moving overlapping grids with adaptive mesh refinement for high-speed reactive and non-reactive flow*, J. Comput. Phys., 216:744–779, 2006. 1
[15] P. Hwang, R. Fedkiw, B. Merriman, T. Aslam, A. Karagozian, and S. Osher, *Numerical resolution of pulsating detonation waves*, Combust. Theory Model., 4:217–240, 2000. 2.3
[16] A. Kurganov, *An accurate deterministic projection method for hyperbolic systems with stiff source term*, in T.Y. Hou and E. Tadmor (eds.), Hyperbolic Problems: Theory, Numerics, Applications, Springer, Berlin, 2003. 1, 2.3, 2.3
[17] A. Kurganov and C.T. Lin, *On the reduction of numerical dissipation in central-upwind schemes*, Commun. Comput. Phys., 2:141–163, 2007. 1
[18] A. Kurganov, S. Noelle, and G. Petrova, *Semidiscrete central-upwind schemes for hyperbolic conservation laws and Hamilton-Jacobi equations*, SIAM J. Sci. Comput., 23:707–740, 2001. 1
[19] A. Kurganov, M. Prugger, and T. Wu, *Second-order fully discrete central-upwind scheme for two-dimensional hyperbolic systems of conservation laws*, SIAM J. Sci. Comput., 39:A947–A965, 2017. 1
[20] A. Kurganov and E. Tadmor, *New high-resolution central schemes for nonlinear conservation laws and convection-diffusion equations*, J. Comput. Phys., 160:241–282, 2000. 1
[21] A. Kurganov and E. Tadmor, *Solution of two-dimensional Riemann problems for gas dynamics without Riemann problem solvers*, Numer. Meth. Partial Differ. Equ., 18:584–608, 2002. 1, 6
[22] R.J. LeVeque and H.C. Yee, *A study of numerical methods for hyperbolic conservation laws with stiff source terms*, J. Comput. Phys., 86:187–210, 1990. 1
[23] G.I. Marchuk, *Splitting and alternating direction methods*, in P.G. Ciarlet and J.L. Lions (eds.), Handbook of Numerical Analysis, I, North-Holland, Amsterdam, I, 1990. 1
[24] H. Nessyahu and E. Tadmor, *Nonoscillatory central differencing for hyperbolic conservation laws*, J. Comput. Phys., 87:408–463, 1990. 6
[25] D. Nguyen, F. Gibou, and R. Fedkiw, *A fully conservative ghost fluid method and stiff detonation waves*, 12th. Int. Detonation Symposium, San Diego, CA, 2002. 1
[26] G. Strang, *On the construction and comparison of difference schemes*, SIAM J. Numer. Anal., 5:506–517, 1968. 1
[27] P.K. Sweby, *High resolution schemes using flux limiters for hyperbolic conservation laws*, SIAM J. Numer. Anal., 21:995–1011, 1984. 6
[28] L. Tosatto and L. Vigevano, *Numerical solution of under-resolved detonations*, J. Comput. Phys., 227:2317–2343, 2008. 1, 3.1
[29] P.N. Vabishchevich, *Additive Operator-Difference Schemes: Splitting Schemes*, De Gruyter, Berlin, 2014. 1
[30] B. van Leer, *Towards the ultimate conservative difference scheme. V. A second-order sequel to Godunov's method*, J. Comput. Phys., 32:101–136, 1979. 6
[31] J.H. Wang, S. Pan, X.Y. Hu, and N.A. Adams, *A split random time-stepping method for stiff and nonstiff detonation capturing*, Combust. Flame, 204:397–413, 2019. 1, 4
[32] W. Wang, C.W. Shu, H.C. Yee, D.V. Kotov, and B. Sjögreen, *High order finite difference methods with subcell resolution for stiff multispecies discontinuity capturing*, Commun. Comput. Phys., 17:317–336, 2015. 1, 4, 5, 5, 6
[33] W. Wang, C.W. Shu, H.C. Yee, and B. Sjögreen, *High order finite difference methods with subcell resolution for advection equations with stiff source terms*, J. Comput. Phys., 231:190–214, 2012. 1, 3.1
[34] F.A. Williams, *Combustion Theory*, Addison-Wesley, Reading, MA, 1965. 1
[35] M. Xiao, G. Ni, C. Wang, and T. Yang, *Front capturing by level set method for the reactive Euler equations*, Int. J. Numer. Meth. Fluids, 93:2723–2743, 2021. 1
[36] H.C. Yee, D.V. Kotov, W. Wang, and C.W. Shu, *Spurious behavior of shock-capturing methods by the fractional step approach: problems containing stiff source terms and discontinuities*, J. Comput. Phys., 241:266–291, 2013. 1, 4
[37] B. Yu, L. Li, B. Zhang, and J. Wang, *An approach to obtain the correct shock speed for Euler equations with stiff detonation*, Commun. Comput. Phys., 22:259–284, 2017. 1, 4, 4.3, 4.3
[38] B. Zhang, H. Liu, F. Chen, and J.H. Wang, *The equilibrium state method for hyperbolic conservation laws with stiff reaction terms*, J. Comput. Phys., 263:151–176, 2014. 1, 3.1, 3.1, 4